1 **Dynamic MJO forecasts using an ensemble subseasonal-to-seasonal**
2 **forecast system of IAP-CAS model**

3 Yangke Liu[1,6], Qing Bao[*1], Bian He[1], Xiaofei Wu[2], Jing Yang[3], Yimin Liu[1], Guoxiong Wu[1], Tao Zhu[1],

4 Siyuan Zhou[1], Yao Tang[1,6], Ankang Qu[1,7], Yalan Fan[3], Anling Liu[3], Dandan Chen[1,6], Zhaoming Luo[1,7],

5 Xing Hu[4], Tongwen Wu[5]

6 [1]State Key Laboratory of Numerical Modeling for Atmospheric Sciences and Geophysical Fluid Dynamics (LASG), Institute

7 of Atmospheric Physics, Chinese Academy of Sciences, Beijing 100029, China

8 [2]School of Atmospheric Sciences/Plateau Atmosphere and Environment Key Laboratory of Sichuan Province, Chengdu

9 University of Information Technology, Chengdu 610225, China

10 [3]Faculty of Geographical Science, Beijing Normal University, Beijing 100875, China

11 [4]National Meteorological Information Center, China Meteorological Administration, Beijing 100081, China

12 [5]Center for Earth System Modeling and Prediction, China Meteorological Administration, Beijing 100081, China

13 [6]College of Earth and Planetary Sciences, University of Chinese Academy of Science, Beijing 100049, China

14 [7]School of Emergency Management Science and Engineering, University of Chinese Academy of Science, Beijing 100049,

15 China

16 *Correspondence to*: Qing Bao (baoqing@mail.iap.ac.cn)

17   **Abstract.** The Madden-Julian Oscillation (MJO) is a crucial predictability source on a sub-seasonal to seasonal (S2S) timescale.

18   Therefore, the models participating in the WWRP/WCRP S2S prediction project focus on accurately predicting and analyzing

19   the MJO. This study provided a detailed description of the configuration within the IAP-CAS S2S forecast system. We assessed

20   the accuracy of the IAP-CAS model's MJO forecast using traditional RMM analysis and cluster analysis. Then, we explained

21   the reasons behind any bias observed in the MJO forecast. Comparing the 20-year hindcast with observations, we found that

22   the IAP-CAS ensemble mean has a skill of 24 days. However, the ensemble spread still has potential for improvement. To

23   examine the MJO structure in detail, we used cluster analysis to classify the MJO events during boreal winter into four types:

24   fast-propagating, slow-propagating, standing, and jumping patterns of MJO. The model exhibits biases of overestimated

25   amplitude and faster propagation speed in the propagating MJO events. Upon further analysis, it was found that the model

26   forecasted a wetter background state. This leads to more intense forecasted convection and stronger coupled winds, especially

27   in the fast MJO events. However, the horizontal moisture advection effect for eastward propagation is overestimated in IAP-

28   CAS due to the wetter state and more substantial MJO circulations, which results in a faster MJO mode. These findings show

29   that the IAP-CAS skilfully forecasts signals of MJO and its propagation, and they also provide valuable guidance for improving

30   the current MJO forecast by developing the ensemble system and moisture forecast.

31   **Keywords**: MJO prediction, S2S, IAP-CAS, FGOALS-f2, Cluster Analysis

1 Introduction

With the increasing occurrence of metrological disasters in recent years, there has been growing attention toward S2S forecast, as it bridges the gap between weather and climate forecasts and reduces disaster risks through early warnings. In November 2013, the WWRP/WCRP S2S prediction project (Phase 1) was launched, with the principal objectives of enhancing S2S forecast accuracy and advancing our comprehension of its dynamics and climate drivers. Then, work on the S2S research continued in Phase 2, from 2018 to 2023. The whole project has made a significant contribution to the development of S2S prediction.

MJO (Madden and Julian, 1971) is a crucial predictability source of S2S forecasts. It is a significant tropical oscillation with a period of 30-60 days, characterized by expansive cloud masses and precipitation systems that propagate eastward along the equatorial regions. Accurate S2S prediction requires a good representation of MJO. Many studies have clarified the relationship between the MJO and global weather and climate, such as monsoons (Goswami, 2012; Hsu, 2012; Lau and Chan, 1986; Wheeler et al., 2009), tropical cyclones (Bessafi and Wheeler, 2006; Ferreira et al., 1996; Hall et al., 2001) and El Niño-Southern Oscillation (ENSO; Lau et al., 2005; Zhang, 2005). The convective and circulation anomalies associated with MJO establish intricate connections across global weather and climate systems on the S2S timescale. Being able to accurately forecast the MJO can have a positive impact on the forecast of other related systems (Cassou, 2008; Vitart and Molteni, 2010; Wu et al., 2007). Achieving an accurate forecast of MJO becomes a primary objective in the field of S2S forecasts.

With an enhanced comprehension of the underlying physical mechanisms governing the MJO and the continuous improvement of numerical models, remarkable advancements have been achieved in the MJO forecast. In Coupled Model Intercomparison Project Phase 6 (CMIP6), models that exhibited lower forecast skills (Hung et al., 2013) in Coupled Model Intercomparison Project Phase 5 (CMIP5) have demonstrated noteworthy improvements in the simulation of MJO (Ahn et al., 2020). Generally, the models in CMIP6 simulate more realistic eastward propagation and precipitation over the Maritime Continent (MC) region (Ahn et al., 2019; Chen et al., 2022).

However, for S2S forecasts, the improvement of model physics is one aspect of advancing S2S forecasts, as various factors impact MJO forecast skills, such as initialization and ensemble generation (Kim et al., 2018). The forecast skills of the MJO in most models is typically 3-4 weeks (Vitart, 2017), while the estimate of predictability of MJO is approximately 5-7 weeks (Waliser et al., 2003; Neena et al., 2014). These facts underscore the persisting challenges in the S2S forecasts.

The realistic forecast of MJO eastward propagation is one of the challenges repeatedly mentioned in recent years (Jiang, 2017; Kim, 2019; Lim et al., 2018; Wang and Lee, 2017). The MJO propagation skill is closely related to the forecast of the state in the Maritime Continent (MC) region (Gonzalez and Jiang, 2017). Many studies have pointed out the "MC barrier" (Hendon and Salby, 1994; Rui and Wang, 1990a; Vitart et al., 2017) during the MJO's propagation through the MC region. The "MC barrier" refers to a notable deterioration of the MJO signal when it traverses the MC area, but this phenomenon is usually

63 amplified in the climate models (Kim et al., 2014b; Neena et al., 2014; Xiang et al., 2022, 2015), showing the model's limitation

64 in preserving MJO propagation within the MC region. The moisture mode theory (Raymond and Fuchs, 2009) has been

65 proposed to explain this phenomenon. It suggests that the advection of seasonal mean moisture by the MJO-related circulation

66 anomalies in the low troposphere is crucial to MJO's propagation through the MC region (Jiang, 2017; Kim, 2019). In models

67 that are hard to capture the realistic propagation of MJO, the mean low-troposphere moisture amplitude over the MC is

68 underestimated, resulting in a weakened horizontal moisture gradient (Gonzalez and Jiang, 2017; Kim, 2017). This discrepancy

69 in moisture advection hinders MJO propagation.

70 The Institute of Atmospheric Physics at the Chinese Academy of Sciences (IAP-CAS) has been actively involved in climate

71 model development and applications since the CMIP1 in the 1990s. As for the IAP-CAS model, it has already shown a

72 significant enhancement in MJO simulation in CMIP6 compared to CMIP5 (Chen et al., 2022), but the performance of the

73 S2S system in IAP-CAS remains uncertain and requires comprehensive evaluation. Therefore, the objectives of this article are

74 fourfold: Firstly, the aim is to introduce the S2S forecast system of the IAP-CAS model. Secondly, to evaluate the forecast

75 skills of the IAP-CAS in the MJO forecast. Thirdly, the aim is to analyze the evaluation results to identify the sources of

76 forecast errors. This will facilitate further improvements in the MJO forecast. At last, we hope that the verification and analysis

77 process can provide some valuable insights for other models.

78 The structure of the paper is as follows. A thorough review of the IAP-CAS model and S2S ensemble forecast system is

79 introduced in Section 2. Section 3 describes the observation data and primary methodology utilized in the article. Section 4

80 assessed the overall MJO forecast skills in IAP-CAS. Section 5 focused on analyzing the propagation details of the fast-

81 propagating and slow-propagating MJO. After that, in Section 6, we discussed the potential causes of any bias observed in the

82 MJO forecast. In Section 7, we summarized our findings and had a discussion.

83 **2 The global S2S ensemble forecast system of IAP-CAS**

84 The architecture of the IAP-CAS S2S ensemble forecast system is depicted in Figure 1. In this section, we will give a thorough

85 description of the S2S system, covering the model, initialization methods, ensemble generation approaches, and the resulting

86 datasets.

87 **2.1 Configuration of IAP-CAS model**

88 The climate system model CAS FGOALS-f2 (The Flexible Global Ocean-Atmosphere-Land System model Finite Volume

89 version 2, Chinese Academy of Sciences; Bao 2019; Bao et al. 2020) is the core of the IAP-CAS S2S ensemble forecast system.

90 It is developed by the State Key Laboratory of Numerical Modeling for Atmospheric Sciences and Geophysical Fluid

91 Dynamics (LASG) at the Institute of Atmospheric Physics (IAP), Chinese Academy of Sciences (CAS). We utilize the

92 institution name, IAP-CAS, as a proxy for the model.

93   FGOALS-f2 is a fully coupled model that encompasses four components: atmospheric, land, oceanic, and sea ice models, with

94   its configuration detailed in Table 1. The atmospheric component is version 2 of the Finite-volume Atmospheric Model

95   (FAMIL2; Li et al. 2019), with a standard horizontal resolution of C96, which means 96×96 grid points in each tile of the

96   cube sphere, roughly equivalent to 1-degree resolution. Vertically, it features 32 hybrid sigma-pressure levels, with the

97   uppermost level situated at 1 hPa (The Hybrid coefficients are listed in Table 2). The land surface component used in FGOALS-

98   f2 is version 4 of the Community Land Model (CLM4.0; Oleson et al. 2010; Lawrence et al. 2011), featuring a horizontal

99   resolution nearly at 1-degree resolution. The oceanic component is Parallel Ocean Program version 2 (POP2; Kerbyson and

100   Jones 2005), which utilizes a displaced-pole grid with the North Pole shifted to Greenland. This grid has a resolution of gx1v6,

101   approximately equivalent to a 1-degree horizontal resolution, and includes 60 vertical layers. The sea ice component is the Los

102   Alamos Sea Ice Model version 4.0 (CICE4; Hunke et al. 2010), sharing the exact horizontal resolution as the ocean model.

103   These four components are coupled via the coupler version 7 in the Community Earth System Model (CESM; Craig et al.

104   2012).

105   It is worth noting that FAMIL2, the latest generation atmospheric model from LASG, has adopted the Finite-Volume Cubed-

106   Sphere Dynamical Core (FV3; Lin 2004; Putman and Lin 2007) as its dynamical core. FV3 solves the fully compressible Euler

107   equations on the gnomonic cubed-sphere grid and a Lagrangian vertical coordinate. Fast vertically propagating sound and

108   gravity waves are solved by the semi-implicit method (Harris et al., 2020). This enhancement of the atmospheric component

109   results in improved computational efficiency and accuracy. Besides, the key parameterization in FAMIL2 is a Resolved

110   Convection Precipitation scheme (RCP), which is independently developed to calculate the microphysics processes in the

111   convective precipitation for both deep and shallow convection (Bao and Li, 2020). Due to the rapid phase changes occurring

112   within the convective cloud, a sub-time step of 150 seconds is employed for the calculation of microphysical processes within

113   a physical timestep of 30 minutes. FAMIL2 has also implemented the University of Washington Moist Turbulence

114   parameterization scheme (UWMT, Park and Bretherton 2009) as its boundary layer scheme. The microphysical

115   parameterization used in FAMIL2 is the revised Lin scheme, which is a single-moment scheme (Zhou et al., 2019).

116   Building upon previous work, it has been observed that the IAP-CAS model can effectively reproduce the patterns and intensity

117   of ENSO variability (Fig. A2), and it also shows a skillful forecast of tropical cyclones (Li et al., 2021, 2022). As mentioned

118   in Section 1, the activity of the MJO is significantly impacted by the tropical weather and climate systems, including ENSO

119   and tropical cyclones (TCs). The accurate forecast of ENSO and TCs heightens our anticipation for MJO forecast skill in the

120   IAP-CAS model. FAMIL2 has already provided a realistic forecast of convectively coupled equatorial waves (CCEWs) and

121   MJO convection (Li et al., 2019). The S2S forecast system also exhibits excellent performance in forecasting arctic sea ice

122   (Liu et al., 2023) and spring rainfall (Fan et al., 2023).

123   **2.2 Initialization scheme of the S2S forecast system**

124   The S2S forecast system of the IAP-CAS model adopts a Newtonian nudging method with time-varying treatment (Jeuken et

125   al., 1996) to complete the initialization of the atmosphere and ocean. The reanalysis nudging and the forecast nudging are the

126   two components that make up the initialization process, which is seen in Figure 2. Table 3 provides a summary of the detailed

127   technical specifics for these two nudging processes.

128   The reanalysis nudging initializes the atmospheric variables, including temperature, surface pressure, sea level pressure, and

129   surface wind from the NCEP Final Operational Global Analysis datasets (FNL, http://rda.ucar.edu/datasets/ds083.2,

130   ds083.2|DOI: 10.5065/D6M043C6). The oceanic variable of potential temperature from the National Oceanic and Atmospheric

131   Administration (NOAA) Optimum Interpolation Sea Surface Temperature (OISST) reanalysis data (Reynolds et al., 2007) is

132   also included. These reanalysis data serve as observations in the eq. (1) to diminish errors in the initial condition:

133    $x(t) = x_{model}(t) + N_{rea}(t)[x_{obs}(t) - x_{model}(t)]$ (1)

134   where t is the time, $x(t)$ is the filed after nudging process, $x_{model}(t)$ represents the model forcing, $x_{obs}(t)$ represents the

135   "truth" value, and $N_{rea}(t)$ is a relaxation coefficient that varies over time, which constantly adjusts the model results during

136   the integration process, making it approximate to the observed values while being constrained by the dynamical constraints of

137   the physical model. The calculation process for $N_{rea}(t)$ is as follows:

138    $N_{rea}(t) = \dfrac{\Delta t}{\frac{T}{1+cos(2\pi \cdot \frac{t\%T}{T})} + \Delta t}$ (2)

139   Δt is the time step in FAMIL2, which is 0.5h for C96 resolution (approximately 1-degree resolution). T represents the time

140   window with a value of 6 hours. As depicted in Figure 2a, the relaxation coefficient varies as a cosine function. It is large at

141   the beginning and end of the temporal window, thereby facilitating accelerated convergence of the model results towards

142   observations. While in the middle of the time window, N_{rea} becomes smaller and even drops to zero, which indicates the

143   reliability of the reanalysis data decreases. The reason is that the reanalysis data within the time window is obtained through

144   interpolation between its start and end values.

145   In the forecast nudging, the initialization process adheres to a similar nudging algorithm at 6-h intervals, as shown in eq. (3).

146    $x(t) = x_{model}(t) + N_{fcst}(t)[x_{fcst}(t) - x_{model}(t)]$ (3)

147   Nevertheless, the atmospheric variables assimilated into the S2S system are sourced from the GFS weather forecast, denoted

148   as $x_{fcst}(t)$. The relaxation coefficient $N_{fcst}(t)$ is as follows:

149    $N_{fcst}(t) = \dfrac{\Delta t}{\frac{T}{1+cos(2\pi \cdot \frac{t\%T}{T})} + \Delta t} \cdot cos(\frac{\pi}{2} \cdot \frac{(t-t\%T)}{4mT})$ (4)

150   Compared to N_{rea}, N_{fcst} is multiplied by a decay factor, which also varies in accordance with the cosine function. In this

151   context, the number of days for forecast nudging is denoted by m, and the system is configured with a 10-day forecast nudging

152   period. Figure 2b illustrates the variation of N_{fcst}, which decreases as the reliability of weather forecast data diminishes over

153   time, ultimately reaching zero by the 10th day.

154   Summarily, the S2S forecast system commences its daily forecast from the initial condition derived via reanalysis nudging. It

155   then fine-tunes the forecasts with weather prediction data through the forecast nudging process. This initialization system

156   effectively reduces system errors in the model and augments forecast accuracy.

2.3 Time-lagged method for ensemble generation

158   The value of ensemble forecasts in medium to long-term forecasts has been repeatedly emphasized (Liu, 2003; Vitart and

159   Molteni, 2009). In addition to improving the physical scheme of the model, devising an effective approach for ensemble

160   generation might have a considerable impact on the MJO forecast. The IAP-CAS S2S ensemble forecast system utilizes the

161   time-lagged method (Hoffman and Kalnay, 1983) to generate ensemble members.

162   A schematic diagram of the time-lagged method is depicted in Figure 2b. During the initial day of the forecast nudging, the

163   S2S system issues forecasts from 00Z, 06Z, 12Z, and 18Z, resulting in the generation of 4 ensemble members. The core idea

164   behind this approach is to introduce perturbations by leveraging lagged initialization times.

2.4 Hindcast experiment and real-time forecast

166   The S2S ensemble forecast system provides daily forecasts, forecasting weather and climate conditions for the upcoming 65

167   days. Out of the 65 days, 5 days are reserved for extending the ensemble members by using the time-lagged method, ensuring

168   a complete forecast for at least 60 days. Since June 1st, 2019, the IAP-CAS S2S system has been operating 16 ensemble

169   members daily for real-time forecast, and for hindcast experiments from 1999 to 2018, it has run 4 ensemble members daily.

170   Our subsequent research is based on the 20-year hindcast experiment.

171   In 2021, the IAP-CAS model participated in phase II of the S2S Project (Vitart et al., 2017) successfully, providing the 20-

172   year hindcast and real-time forecast data generated by the S2S ensemble forecast system. Detailed information regarding the

173   data is listed in Table 4, and Table 5 shows the list of output variables. The output data is interpolated to a standardized

174   horizontal resolution of 1.5°×1.5°, following the S2S's requirements, and is stored in version 2 of General Regularly-distributed

175   Information in Binary (GRIB2) format. The output data of the S2S system is publicly available on three S2S Data Portals

176   (ECMWF, CMA, and IRI).

3 Datasets and methods

3.1 datasets

179   The observational datasets used for the MJO verification include the NOAA daily outgoing longwave radiation (OLR;

180   Liebmann and Smith 1996), daily wind from the National Centers for Environmental Prediction (NCEP)/Department of Energy

181   (DOE) Reanalysis 2 dataset (Kanamitsu et al., 2002), daily specific humidity from ECMWF Reanalysis version 5 (ERA5;

182   ERA 2017), and the precipitation product from the Global Precipitation Climatology Project (GPCP; Adler et al. 2003). To

183   facilitate computation and meaningful comparisons, both observation and hindcast datasets have been uniformly interpolated

184   to a horizontal resolution of 2.5°×2.5°. Seven pressure levels (1000, 925, 850, 700, 500, 300, and 200hPa) of wind and specific

185   humidity are extracted for analysis.

186   **3.2 MJO RMM index**

187   To conduct a quantitative assessment of MJO, we have employed the widely used Real-time Multivariate MJO (RMM) index

188   (Wheeler and Hendon, 2004a) to extract the MJO signal. This index consists of two components, RMM1 and RMM2, which

189   are the first and second principal components of the combined empirical orthogonal functions (EOFs) of multiple variables,

190   including OLR, 200hPa zonal wind (U200), and 850hPa zonal wind (U850). It serves as a tool for tracking the location and

191   amplitude characteristics of MJO.

192   The calculation of the RMM index refers to the method described in Gottschalck et al. (2010). Detailed calculation steps are

193   as follows:

194   1)   Remove the 0-3 waves of the climatology and low-frequency variability of the U200, U850, and OLR variables from both

195   the observation and hindcast data. It is noteworthy that removing low-frequency variability is to subtract the mean of the

196   past 120 days from the anomalies. For model forecast, this is the mean model anomalies of the previous forecast days,

197   plus the mean observed anomalies of the remaining days.

198   2)   Average the anomalies between 15° S and 15° N and normalize the three variables, using the pre-computed coefficients

199   as in Gottschalck et al. (2010).

200   3)   Project the anomalies onto the observed combined EOF eigenvectors from Wheeler and Hendon (2004b) to get RMM1

201   and RMM2.

202   Bivariate anomaly correlation coefficient (ACC) and bivariate root mean square error (RMSE) are calculated using the

203   observed and hindcast RMM indices to represent the forecast skills of the IAP-CAS model as

204     $ACC(\tau) = \frac{\sum_{t=1}^{N}[a_1(t)b_1(t,\tau)+a_2(t)b_2(t,\tau)]}{\sqrt{\sum_{t=1}^{N}[a_1^2(t)+a_2^2(t)]}\sqrt{\sum_{t=1}^{N}[b_1^2(t,\tau)+b_2^2(t,\tau)]}}$, and   (5)

205     $RMSE(\tau) = \sqrt{\frac{1}{N}\sum_{t=1}^{N}[(a_1(t)-b_1(t,\tau))^2 + (a_2(t)-b_2(t,\tau))^2]}$ (6)

206   Here $a_1(t)$ and $a_2(t)$ are the observation RMM1 and RMM2 at time t; $b_1(t)$ and $b_2(t)$ are the forecasting RMM1 and

207   RMM2 at time t for lead τ days; N is the total number of times. It is commonly accepted that days with ACC above 0.5 are

208   considered to have valid forecasts. Therefore, the forecast skill of a model is quantitively defined as the maximum lead time

209   exceeding 0.5, which approximately corresponds to the day when RMSE reaches $\sqrt{2}$.

210   RMM index can also be adapted to quantitively evaluate the forecasted intensity and velocity through the calculation of the

211   error of amplitude ($ERR_{amp}(\tau)$) and phase ($ERR_{phase}(\tau)$) as a function of lead time τ:

212     $ERR_{amp}(\tau) = \frac{1}{N}\sum[AMP_b(t,\tau) - AMP_a(t)]$, and   (7)

213     $ERR_{phase}(\tau) = \frac{1}{N}\sum tan^{-1}[\frac{a_1(t)b_2(t,\tau)-a_2(t)b_1(t,\tau)}{a_1(t)b_1(t,\tau)+a_2(t)b_2(t,\tau)}]$ (8)

214   Negative (positive) $ERR_{amp}(\tau)$ indicates weaker (stronger) amplitude in forecasts. Similarly, Negative (positive)

215    $ERR_{phase}(\tau)$ indicates slower (faster) propagation in forecasts. Here the MJO amplitude for observation ($AMP_a(t)$) and

216   forecast ($AMP_b(t)$) is defined as

217    $AMP_a(t) = \sqrt{a_1(t)^2 + a_2(t)^2}$, and   (9)

218    $AMP_b(t,\tau) = \sqrt{b_1(t,\tau)^2 + b_2(t,\tau)^2}$.   (10)

219   **3.3 Cluster analysis of MJO events**

220   Another crucial method used in this research is the cluster analysis. In Section 5, we select the representative MJO events

221   and classify them following the work Wang et al. (2019) did. This facilitates a more focused and targeted investigation into

222   the forecast bias of MJO in the IAP-CAS model.

223   An MJO event was chosen if the regional average of OLR, spanning from 10° S to 10° N and 75° E to 95° E, remained

224   below one standard deviation for a consecutive period of 5 days during the boreal winter (November–April). Subsequently,

225   the K-means cluster analysis is employed to categorize the chosen MJO events based on the propagation patterns from day -

226   10 to 20 (day 0 is the day with the peak MJO in the Indian Ocean). At last, we use silhouette clustering evaluation criteria to

227   identify and eliminate poorly classified MJO events.

228   Finally, a total of 50 MJO events were selected from 1999 to 2018 winter and four types of MJO events were identified,

229   namely the fast-propagating (10 cases), slow-propagating (16 cases), standing (12 cases), and jumping (12 cases) patterns of

230   MJO (Fig. 5).

231   The fast-propagating MJO and slow-propagating MJO belong to the propagating type of MJO, characterized by their

232   consecutive eastward propagation across the Indian Ocean to the Pacific Ocean region. On the other hand, the standing and

233   jumping MJO represent relatively non-propagating types, where the convection remains relatively fixed or exhibits

234   inconsecutive movement. Wang et al. (2019) believe that propagating MJO events are often associated with strong and

235   tightly coupling Kelvin waves, especially for fast-propagating MJO. This is the biggest difference between propagating MJO

236   and non-propagating MJO.

237   **4 Evaluation of MJO forecast skill from the IAP-CAS model**

238   Figure 3 demonstrates the overall MJO forecast skill in the IAP-CAS model and the improvement brought by the time-lagged

239   ensemble method. Figure 3a shows the forecast skill of the ensemble mean is 24 days with the criterion of ACC exceeding 0.5,

240   while the skill of individual members is about 21-22 days. Meanwhile, the ensemble mean RMSE reaches $\sqrt{2}$ at 21 days and

241   the individual members exhibit larger RMSE, reaching $\sqrt{2}$ at 16 days (Fig. 3b). The solid blue line in Figure 3b represents the

242   ensemble spread (Leutbecher and Palmer, 2008) of IAP-CAS. When this ensemble spread approaches the RMSE of the

243   ensemble mean (solid red line), it indicates that the ensemble members are sufficiently dispersive. Figure 3b illustrates that the

244   ensemble exhibits an underdispersive characteristic in the early stage of the forecast. We have also observed similar issues of

245   " underdispersive" in many other models (Rashid et al., 2011; Neena et al., 2014; Kim et al., 2014b; Xiang et al., 2015), and

246   addressing this aspect may be a focal point for future model enhancements.

247   Increasing the number of ensemble members within a certain range proves effective in forecasting the uncertainty of weather

248   and climate (Hou et al. 2001). We employed the time-lagged ensemble method to further augment the ensemble members. The

249   time-lagged ensemble includes the ensemble members generated on the forecast day and from lag times. For instance, by

250   incorporating ensemble members with a lag of i ($i = 0, 1, 2, ...$) days, the total number of members becomes $4 * (i + 1)$.

251   Upon examining the relationship between lag i days and forecast skill, it was found that the skill increases as i increases at

252   first, but then it reaches a plateau when $i > 3$ (see Fig. A3). This suggests that the forecast skill of the 16 members may

253   represent the limit of the time-lagged ensemble method in IAP-CAS. Figure 3d shows the ensemble of 16 members is more

254   dispersive than 4 members, which is illustrated by less distinction between RMSE and Spread in the 16-member system. The

255   ensemble mean of 16 members achieves a skill of 26 days, surpassing the skill of 4 members by two days (Fig. 3c).

256   Numerous prior investigations have demonstrated that MJO forecast skill is sensitive to the MJO amplitude in many models

257   (Lin et al., 2008; Rashid et al., 2011; Wang et al., 2014; Xiang et al., 2022), and this characteristic is also evident in the IAP-

258   CAS model. We classify an MJO case as an initial (target) strong case if its initial (target) amplitude is greater than 1, while

259   an event with an initial (target) amplitude less than 1 is classified as an initial (target) weak case. Figures 4a-b show that in the

260   IAP-CAS model, the forecast skills of strong MJO cases are generally higher than weak cases, especially in the target strong

261   (weak) cases.

262   The amplitude and phase of MJO serve as additional indicators for a detailed assessment of MJO forecast performance. For

263   initially strong MJO cases, we analyze the MJO amplitude and forecasted phase angle error (Figs. 4b-c). The individual

264   member has a stronger amplitude than observation, which leads to a relatively strong amplitude in the ensemble mean during

265   the initial 40 days. However, as the noise rapidly increases, the phase error of the individual members also escalates (as shown

266   in Fig. 4c). The phase error results in a mutual cancellation in positive and negative phases of MJO among ensemble members,

267   leading to a rapid weakening of the amplitude in the ensemble mean. In Figure 4d, the phase error of the ensemble mean

268   indicates that the speed of forecasted MJO tends to decrease at first and then start increasing around the 10th day. A more

269   detailed investigation into the speed of propagating MJO events will be described in Section 5.

270   **5 The forecast of MJO propagation**

271   We present a qualitative diagnostic of a 20-year hindcast experiment to evaluate the overall forecast skills of IAP-CAS in

272   Section 4. This analysis provides us with preliminary insights into the performance and biases of the system. Based on Wang

273   et al. (2019), we aim to conduct further investigations into different types of MJO events to explore the physical explanation

274   of system biases.

275   In Section 3, we have already described the methodology for classifying MJO events and results. Figure 5 compares the

276   composited propagation patterns of precipitation and U850 between observation and forecast initiated at day -5 for four

277   different MJO types. The fast-propagating and slow-propagating MJO exhibit a consecutive eastward propagation structure

278   from the Indian Ocean across the MC region to the Pacific Ocean. The basic distinction between the two types is that the first

279   type of MJO exhibits a faster propagation speed compared to the second type. The standing MJO remains relatively stationary

280   over the Indian Ocean and does not continue to propagate eastward. The jumping MJO shows a convective system that

281   bypasses the MC region and directly jumps from the Indian Ocean to the Pacific Ocean. Here, fast MJO and slow MJO are

282   considered propagating MJO events, while the latter two types are regarded as non-propagating MJO events.

283   The observed U850 displays a coupled structure characterized by equatorial westerly anomalies of the Kelvin wave component

284   located west of the convection, and easterly anomalies of the Rossby wave component located east of the convection (Rui and

285   Wang, 1990b; Adames and Wallace, 2014; Wang and Lee, 2017). As illustrated in Figure 5, a distinct contrast between

286   propagating MJO and non-propagating MJO can be found in the circulation at the low level: in the propagating MJO events,

287   the Kelvin wave response is strong and tightly coupled with the center of convection, which is shown in the stronger and

288   eastward-extending easterly wind component, particularly prominent in fast MJO events. Many previous studies (Benedict

289   and Randall, 2007; Hsu and Li, 2012; Wang and Lee, 2017) have also indicated that the presence of low-level easterly winds

290   is a key signal that contributes to the eastward propagation of MJO by inducing low-level convergence and premoistening to

291   the east of the major convection. In the non-propagating MJO events, the easterly wind is weak and tends to decouple from

292   the major convection.

293   From the Hovmöller diagram of observed propagating MJO (Fig. 5), a significant change in convection is observed after

294   crossing the MC region, which is marked by a decrease in intensity and a slower propagation speed. This change is roughly

295   delineated by the 135° E, which is commonly referred to as the "MC barrier". As mentioned above, the "MC barrier" effect is

296   usually amplified in the climate models. This phenomenon is also observed in the forecast of slow MJO events in the IAP-

297   CAS model. The forecasted convective signal of slow MJO gradually fades after crossing the MC. However, in the forecast of

298   fast MJO, the convection does not exhibit a significant decrease in intensity after crossing the MC region, and the speed of the

299   propagation appears to be relatively faster compared to observations in both fast and slow MJO events. Figure 5 also shows

300   that the forecast for standing MJO remains somewhat imprecise. The forecasted convection is weak, and there are signals in

301   both the Indian Ocean and the Pacific Ocean, whereas observed standing MJO only indicates strong convective signals in the

302   Indian Ocean. This aspect is also evident in Figure A4, where the standing MJO has the lowest skill (13 days). For each MJO

303   type, we consider the skill as the ACC of the cases initiated from day -20 to day 15 (Xiang et al., 2015). Figure A4 displays

304   that the fast MJO achieves the highest skill at 32 days, while the jumping MJO and slow MJO exhibit skills of 23 and 21 days,

305   respectively.

306   In this work, we focus specifically on the analysis of propagating MJO events which have relatively complete propagation

307   processes. Figures 6 and 7 present the evolution patterns of propagating MJO. It is noticeable in both the spatial propagation

308   diagram (Fig. 6) and the phase diagram (Fig. 7) that the forecasted precipitation intensity is significantly higher than the

309   observed, indicating the presence of a stronger convective system of forecasted fast MJO. The forecasted location of the major

310   convection is relatively biased towards the east (Fig. 6b), which means there is an overestimation of the propagation speed.

311   The phase diagram also indicates a higher speed, with the blue points propagating faster than the red points (Fig. 7a). On the

312   15th day, the MJO convective system crosses the MC region and reaches the eastern Pacific (Figs. 6a-b). It is worth noting

313   that the forecasted negative phase of MJO exhibits a significant development, with an accelerated speed, gradually intruding

314   into the positive phase. By the 20th day, the development of the negative phase has further intensified, extending its influence

315   into the tropical eastern Pacific region, while in the observation, the negative phase remains east of the MC region. A similar

316   phenomenon is also evident in the forecasts of slow MJO events. Figures 6c-d and 7b show that the amplitude of slow MJO is

317   weaker than fast MJO. There are still biases of stronger convection and faster propagation in the forecast of slow MJO. In the

318   later stages, as the negative phase intrudes, the forecasted convective signal in the positive phase is almost absent due to the

319   inherently weaker convection in slow MJO. This amplification of the "MC barrier" in the forecast of slow MJO may contribute

320   to the diminished convective signal. The intrusion of negative-phase convection is also observed in forecasted fast MJO.

321   However, due to the relatively strong positive-phase convection in the forecast of fast MJO, it is less evident in the zonal mean,

322   as shown in the Hovmöller diagram.

6 The possible physical explanation for the forecast biases

324   Section 5 highlights some biases observed in the forecast of propagating MJO, which includes stronger amplitude and faster

325   propagation speed in the IAP-CAS model. These biases are also mentioned in Section 4. In this section, we aim to unravel the

326   physical mechanisms underlying these biases.

327   As a large-scale convective system, MJO's genesis, evolution, and dissipation are intricately linked to atmospheric moisture

328   (Wang, 1988; Kemball-Cook and Weare, 2001; Maloney, 2002; Wang and Lee, 2017). Given that the model forecasts exhibit

329   a systematic bias of stronger amplitude, we start with the diagnosis of the background state in moisture. Figure 8 shows the

330   winter mean specific humidity averaged over 10° S–10° N. A clear positive bias of the background moisture state in the IAP-

331   CAS model is observed (Fig. 8c), which can enhance the convection in the MJO. However, the distribution of this moisture

332   bias is non-uniform. Figure 8c illustrates that the positive moisture bias is more pronounced towards the western Indian Ocean

333   and the central-eastern Pacific, and this bias gradually spreads to the upper levels. However, in the MC region, the positive

334   moisture bias is smaller and primarily concentrated in the low level. We speculate that higher evaporation fluxes in the model

335   may be the reason for the positive moisture bias. Furthermore, the reduction in oceanic surface area within the MC region

336   contributes to a decrease in this positive bias.

337   Figure 9 displays the precipitation-induced condensational heating (Q_2) during fast MJO and slow MJO events. The

338   condensational heating serves as a proxy for the distribution of convection, which was estimated by the moisture sink defined

339   as

340    $$Q_2 = -L_v(\frac{\partial q}{\partial t} + \vec{V} \cdot \nabla q + \omega \frac{\partial q}{\partial p}),$$ (11)

341   where q is the specific humidity, $\vec{V}$ is the horizontal circulation, ω is vertical pressure velocity, and L_v is the latent heat

342   at condensation, which is a constant here. The vertical distribution of Q_2 reveals that both fast MJO and slow MJO events in

343   the model forecasts trigger stronger convection, particularly in the fast MJO events. Furthermore, the enhanced convective

344   heating leads to a strong response in the coupled MJO-related circulation (Fig. 9). On the 10th day, both the fast MJO and the

345   slow MJO experience further intensification in the model. This intensification can be attributed to the amplification of the

346   positive moisture bias following the departure from the MC region.

347   To further understand the faster propagation of MJO in the IAP-CAS model, it is necessary to comprehend the underlying

348   physical processes associated with the propagation of MJO. Under the framework of "moisture mode", Jiang (2017) performed

349   a moisture budget analysis on the latest generation of general circulation models (GCMs) and identified the key processes for

350   the eastward propagation of MJO. This research revealed that the advection ($\vec{V'} \cdot \nabla \bar{Q}$) of the seasonal mean moisture ($\bar{Q}$) by

351   the MJO anomalous circulations ($\vec{V'}$) plays a crucial role in the propagation of MJO. By increasing moisture eastward and

352   decreasing it westward of the MJO convection, the advection regulates the propagation. (Kim et al., 2014a; Adames and Kim,

353   2016; Jiang et al., 2018). Among the two determining factors ($\vec{V'}$ and $\bar{Q}$), the role of the moisture gradient term is further

354   emphasized. Many studies (Gonzalez and Jiang, 2017; DeMott et al., 2018; Ahn et al., 2020) have demonstrated that the mean

355   moisture's horizontal gradient plays a crucial role in determining the propagation of MJO (Fig. 10a). It is well-forecasted in

356   the models that simulate MJO well, leading to realistic horizontal mean moisture gradients and, thus, well-forecasted horizontal

357   moisture advection associated with the MJO (Hsu and Li, 2012; Kim et al., 2014a; Nasuno et al., 2015; Adames and Wallace,

358   2015; Gonzalez and Jiang, 2017). The IAP-CAS model is capable of reproducing this gradient, although there is an overall

359   stronger moisture bias (Fig. 10b). Here, the $\bar{Q}$ presented is the winter mean specific humidity at 850 hPa ($\bar{Q}_{850}$). Research has

360   indicated that the $\bar{Q}_{850}$ is representative (Kim, 2019), and subsequent analysis also focuses on the 850 hPa level.

361   Figure 11 shows the composite equatorial U850 averaged over the 15° S-15° N for fast MJO and slow MJO respectively. It

362   depicts the transition from westerly to easterly winds in the MC region (as enclosed by the two blue dashed lines), leading to

363   the change from positive advection to negative advection. On the 1st and 5th days, the MC region is predominantly occupied

364   by easterly winds, while from the 10th to the 20th day, the region is primarily characterized by westerly winds in both fast MJO

365   and slow MJO. However, the forecasted amplitude of low-level wind is significantly stronger, which can be caused by the

366   enhanced MJO convection as explained earlier.

367   The MJO anomalous circulation patterns in the MC region result in a positive moisture advection on the eastern part of the

368   MJO during the early stages of MJO's development, which facilitates the propagation of convection in the positive phase. We

369   refer to this process as the "developing phase". Figure 12 provides a detailed illustration of this process. Conversely, during

370   the later stages, there is a negative moisture advection on the western side of the MJO, which leads to the propagation of

371   convection in the negative phase and promotes the dissipation of the MJO. We refer to this process as the "decaying phase"

372   (Fig. 12). Compared to the observation, the stronger amplitude of the low-level moisture advection ($\overrightarrow{V'} \cdot \nabla \bar{Q}$) in the model

373   explains the accelerated positive phase of convection during the early stages and the accelerated negative phase during the

374   later stages (Fig. 13). This explains the increasing propagation speed of the forecasted MJO. In the observation, the amplitude

375   of the moisture advection during fast MJO events is stronger than that during slow MJO events, further confirming this physical

376   explanation.

377   In addition to examine the winter mean moisture state ($\bar{Q}$), we have analyzed MJO-related moisture anomalies (Q') as well

378   (Fig. 14). By comparing the evolution pattern of moisture anomalies between slow MJO and fast MJO, it is found that the

379   moisture anomalies in the eastern part of fast MJO are more intense compared to the slow MJO. This results in stronger low-

380   level moisture transport towards the convective region, thereby also facilitating the intensification and acceleration of the MJO.

381   Moreover, there is a significant distinction in the spatial correlation between fast and slow MJO and it happens as early as the

382   1st day. As the forecast lead time progresses, the accuracy of the moisture forecast deteriorates, while fast MJO events display

383   comparatively better performance. The disparity in moisture anomalies is possibly a pivotal factor contributing to differences

384   in forecast skills between the fast (32 days) and the slow MJO (21 days). This underscores the significance of improving

385   moisture forecast in the MJO forecast.

386   **7 Summary and discussion**

387   **7.1 Summary**

388   The graphical abstract presents a workflow for this paper, outlining the structure of this work. This study introduces a newly

389   developed S2S ensemble forecast system of the IAP-CAS model. The introduction primarily focuses on the numerical model,

390   initialization, ensemble generation, and post-processing aspects of the S2S system. Then we aim to identify potential

391   possibilities for developing this S2S system through a comprehensive assessment of its forecast skills. Based on the 20-year

392   hindcast experiment, the IAP-CAS model shows comparable skill (24 days) to other S2S models. However, the ensemble

393   forecast for MJO has been demonstrated to be underdispersive. A detailed examination of the propagating MJO forecasted in

394   the IAP-CAS model reveals that the amplitude of the convection is overestimated with an increasing propagation speed,

395   particularly in the fast MJO events. These biases are accompanied by a faster dissipation of the MJO.

396   The root cause of these biases lies in the model's wetter environment, which leads to enhanced convection and strengthened

397   circulation coupled with convection, and subsequently, stronger moisture convection. The increasing propagation speed in the

398   MJO propagation is mainly associated with the stronger amplitude of the low-level moisture advection ($\overrightarrow{V'} \cdot \nabla \bar{Q}$) in the forecast.

399   Moreover, the differences in forecast skills between the fast MJO and the slow MJO may be attributed to discrepancies in

400   moisture anomalies (Q') forecast. This further underscores the significance of accurate moisture forecasts.

401   **7.2 Discussion**

402   In Figs A5, we compare the forecast skill of the IAP-CA model with ten other S2S models. The MJO index of 11 S2S models

403   and ERA-Interim from the S2S website (http://www.s2sprediction.net/) is used for evaluation during the standard hindcast

404   period 1999-2010. Among the 11 S2S models, the IAP-CAS model exhibits MJO skill above the mean skill level, while the

405   ECMWF model stands out as the highest-performing model. Figure A5b shows that the skill of individual members in ECMWF

406   is approximately 17-18 days, whereas the ensemble mean demonstrates an extended skill of up to 30 days. This phenomenon

407   may be attributed to the ECMWF model's considerable dispersion (Fig. A5c), which once again underscores the critical role

408   of ensemble dispersion in forecasting uncertainties of weather and climate.

409   Therefore, the forthcoming phase in our model's development plan encompasses increasing model dispersion through

410   improved ensemble perturbation methods, with the ultimate goal of improving model forecast skills. The method of orthogonal

411   conditional nonlinear optimal perturbations (CNOPs, Mu et al. 2003) and the second-order exact sampling (Pham, 2001) are

412   both promising approaches for generating initial perturbations in the model. This method allows the generation of a set of

413   initial perturbations in different orthogonal perturbation subspaces, each with the maximum potential for nonlinear

414   development. When applied to ensemble forecast using a simple Lorenz-96 model, the CNOPs method has demonstrated

415   higher forecast skill compared to the commonly used linear Singular Vectors (SVs) method (Lorenz, 1996). Furthermore,

416   PDAF (Parallel Data Assimilation Framework, Nerger et al., 2020) provides an efficient method known as second-order exact

417   sampling, which uses the long-time variability of the model dynamics to estimate the uncertainty. Evidence has already

418   suggested that the use of second-order exact sampling can greatly improve the skill in sea ice extent throughout the Arctic and

419   along the Northern Sea Route (Yang et al., 2020). We plan to explore the application of CNOPs and second-order exact

420   sampling in the IAP-CAS model in the future and eagerly anticipate the potentially significant results it may yield. Additionally,

421   using machine learning to improve the skill of ensemble forecast is also a viable way to enhance the ensemble forecast of our

422   model.

423   In addition to exploring ensemble perturbations, we also intend to enhance the initialization system of the model. Recognizing

424   the moisture is crucial in the forecast of MJO and acknowledging the issue of moisture bias in the IAP-CAS model, it is

15

425 essential to take measures to ameliorate moisture forecast in our model. The recent research by Zeng (Zeng et al., 2023)

426 provides convincing evidence that humidity initialization can indeed significantly enhance MJO forecast in the IAP-CAS S2S

427 forecast system, especially in the 2 and 3 phase of MJO propagation. However, it is worth noting that changes in the mean

428 state have a significant impact on MJO development (Hannah et al., 2015; Kim, 2019), we must pay attention to the influence

429 of moisture initialization on the mean state. Moreover, the current S2S system's initialization process uses the nudging method,

430 and it is worthwhile to explore more efficient methods to enhance the initialization process.

431 We are also considering increasing the resolution of the model to C384 (25 km) globally. A High-resolution coupled model

432 could better represent the MJO (Crueger et al., 2013). This improvement could be attributed to the enhanced resolution, which

433 better captures the ocean-atmosphere interaction – a critical factor for MJO convection. Increasing the resolution is also

434 meaningful for addressing the MC barrier issue because one of the factors contributing to the MC barrier is terrain distortion

435 (Hsu and Lee, 2005; Inness and Slingo, 2006; Wu and Hsu, 2009). Further optimizing the model's physical processes and

436 dynamic-physical coupling is also believed to enhance the forecast of the MJO (Zhou and Harris, 2022). As the foreseeable

437 resolution and complexity of the model increase in the future, the issue of power consumption on X86 architecture processors

438 for handling the growing amount of data will become more pronounced. We have plans to port the model to the computing

439 platform based on ARM architecture to address the challenges posed by the explosive growth of data.

440 **Table 1 Configuration of the coupled climate system model CAS FGOALS-f2**

Component	Model name	Horizontal Resolution	Vertical levels	Reference
Atmosphere	FAMIL2	Cubed Sphere Grid (C96, ~1°×1°)	32 in the hybrid levels	Li et al. 2019
Land	CLM4.0	Nested subgrid hierarchy (f09, ~1°×1°)	15 soil levels and 3 snow levels	Oleson et al. 2010; Lawrence et al. 2011
Ocean	POP2	Displaced-pole grid (gx1v6, ~1°×1°)	60 levels	Kerbyson and Jones 2005
Sea ice	CICE4	Displaced-pole grid (gx1v6, ~1°×1°)	5 levels	Hunke et al. 2010

441   **Table 2 Hybrid coefficient of hybrid sigma-pressure coordinates at layer interfaces in CAS FGOALS-f2**

Layer	Coefficient of pressure coordinates	The coefficient of sigma coordinates	Layer	Coefficient of pressure coordinates	The coefficient of sigma coordinates
1	100.00	0.00	18	27131.33	0.23
2	400.00	0.00	19	24406.11	0.32
3	818.60	0.00	20	21326.05	0.42
4	1378.89	0.00	21	18221.18	0.51
5	2091.80	0.00	22	15275.15	0.59
6	2983.64	0.00	23	12581.68	0.67
7	4121.79	0.00	24	10181.43	0.73
8	5579.22	0.00	25	8081.90	0.79
9	7419.79	0.00	26	6270.87	0.83
10	9704.83	0.00	27	4725.35	0.87
11	12496.34	0.00	28	3417.39	0.91
12	15855.26	0.00	29	2317.75	0.93
13	19839.62	0.00	30	1398.09	0.96
14	24502.73	0.00	31	632.50	0.98
15	28177.10	0.02	32	0.00	0.99
16	29525.28	0.06	33	0.00	1.00
17	29016.34	0.14			

442   **Table 3 Initialization information of the S2S ensemble forecast system**

Nudging type	Data Assimilation	Variable	Data	Frequency
Reanalysis nudging	Time-Lagged Nudging (Hoffman and Kalnay, 1983; Jeuken et al., 1996)	U, V, T, P_s, z_s [a]	FNL (http://rda.ucar.edu/datasets/ds083.2, ds083.2|DOI: 10.5065/D6M043C6)	6h
		SST	NOAA OISST (Reynolds et al., 2007)	
Forecast nudging		U, V, T, P_s, z_s	GFS weather forecast	6h

443   [a] Table notes: U represents zonal wind, V represents meridional wind, T represents temperature, P_s represents surface pressure,

444   z_s represents surface geopotential height, and SST represents sea surface temperature.

445 **Table 4 Introduction to the output data of the S2S ensemble forecast system**

Experiment	Ensemble members	Time range	Frequency	Forecast time	Variable	Resolution	Interpolation method
Hindcast	4	1999-2018	Daily	65 days	25 variables (A detailed list of variables is shown in Table 5)	Horizontal:1.5° ×1.5° Vertical:7 levels (1000, 925, 850, 700, 500, 300, and 200hPa)	One-order conservation
Real-time forecast	16	2019					

446   **Table 5 List the output variables in the S2S ensemble forecast system**

Statistical process	Level(s)	Short name	Standard name	Unit
Instantaneous value/24h	The variables are located on 10 pressure layers (1000, 925, 850, 700, 500, 300, 200, 100, 50, 10 hPa)	gh	Geopotential height	gpm
		t	Temperature	K
		u	U-velocity	m s^{-1}
		v	V-velocity	m s^{-1}
		w	Vertical velocity	pa s^{-1}
	The variable is located on 7 pressure layers (1000, 925, 850, 700, 500, 300, 200 hPa)	q	Specific humidity	kg kg^{-1}
	2-dimensional variables	w	Vertical velocity	pa s^{-1}
		sp	Surface pressure	Pa
		lsm	Land sea mask	Proportion of land
		orog	Orography	gpm
Daily average value		tcc	Total cloud cover	%
		skt	Skin temperature	K
		2t	Surface air temperature	K
		2d	Surface air dewpoint temperature	2d
		wtmp	Sea surface temperature	K
		ci	Sea ice cover	proportion

24-hour accumulated value	sf	Snow fall water equivalent	kg m^{-2}
	ttr	Time-integrated top net thermal radiation	W m^{-2} s
	ssr	Time-integrated surface net solar radiation	W m^{-2} s
	str	Time-integrated surface net thermal radiation	W m^{-2} s
	ssrd	Time-integrated surface solar radiation downwards	W m^{-2} s
	strd	Time-integrated surface thermal radiation downwards	W m^{-2} s
Instantaneous value/6h	mx2t6	Surface air maximum temperature	K
	mn2t6	Surface air minimum temperature	K
	10u	10 metre u-velocity	m s^{-1}
	10v	10 metre v-velocity	m s^{-1}
6-hour accumulated value	tp	Total precipitation	kg m^{-2}
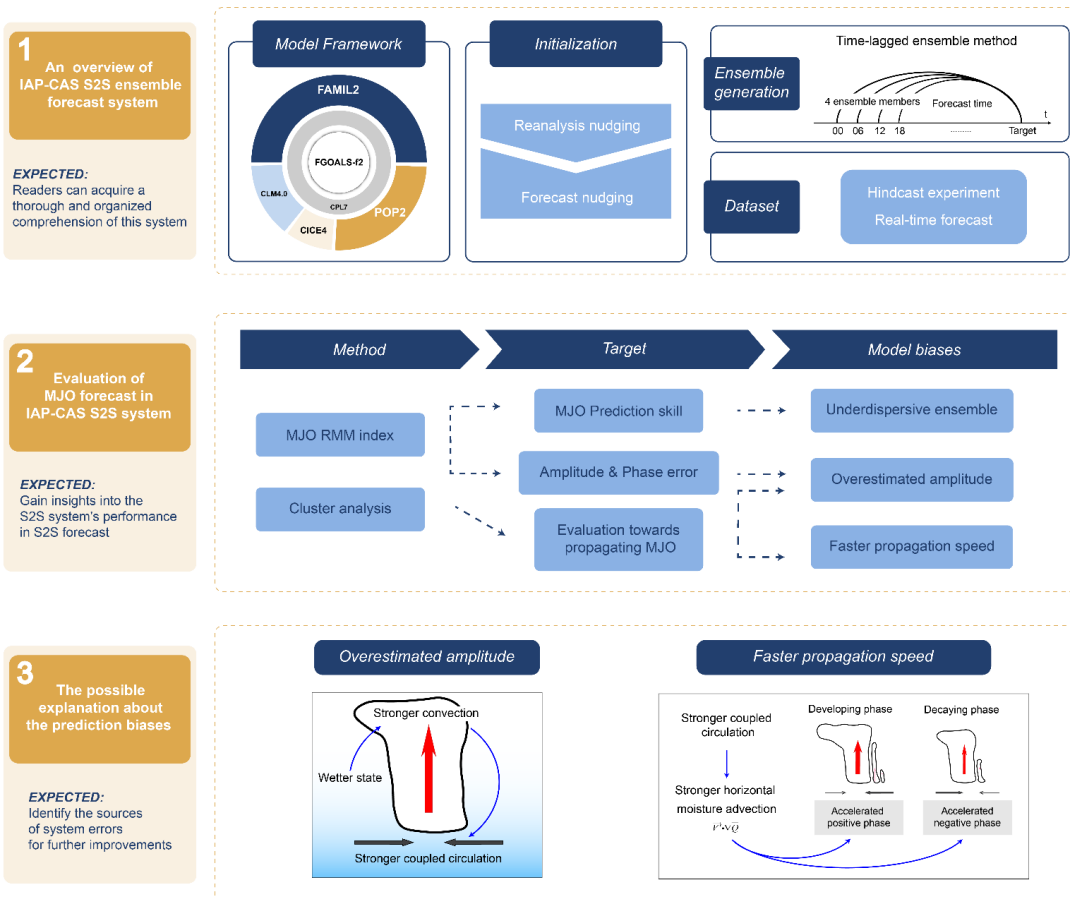
447
448   **The graphical abstract**
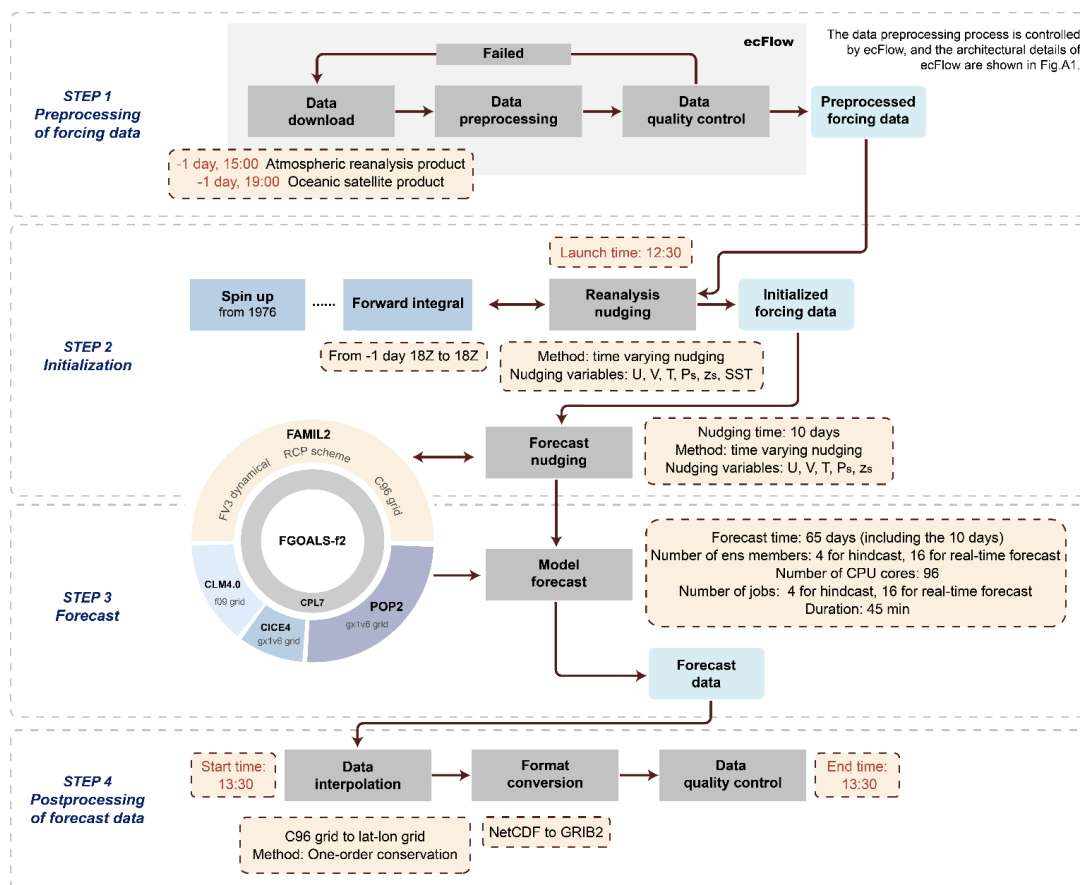
The time marked in red here is local time (beijing time)

Figure 1. The structure of the IAP-CAS S2S ensemble forecast system

451
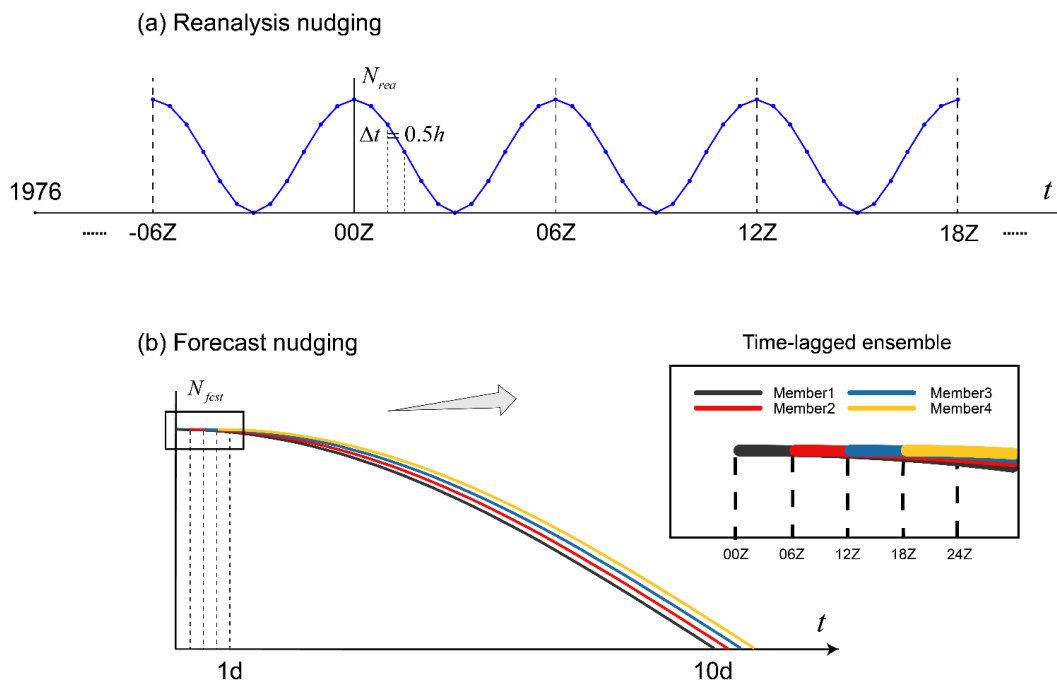
Figure 2. The initialization scheme of the S2S ensemble forecast system in the IAP-CAS model. The relaxation coefficient (N) as a function of time (t) in (a) the reanalysis nudging and (b) the forecast nudging. In (a), The reanalysis nudging begins on January 1, 1976. The dots indicate the nudging process every 30 minutes. In (b), the solid lines of 4 colors represent the 4 ensemble members with their generation facilitated through the application of the time-lagged method.

456
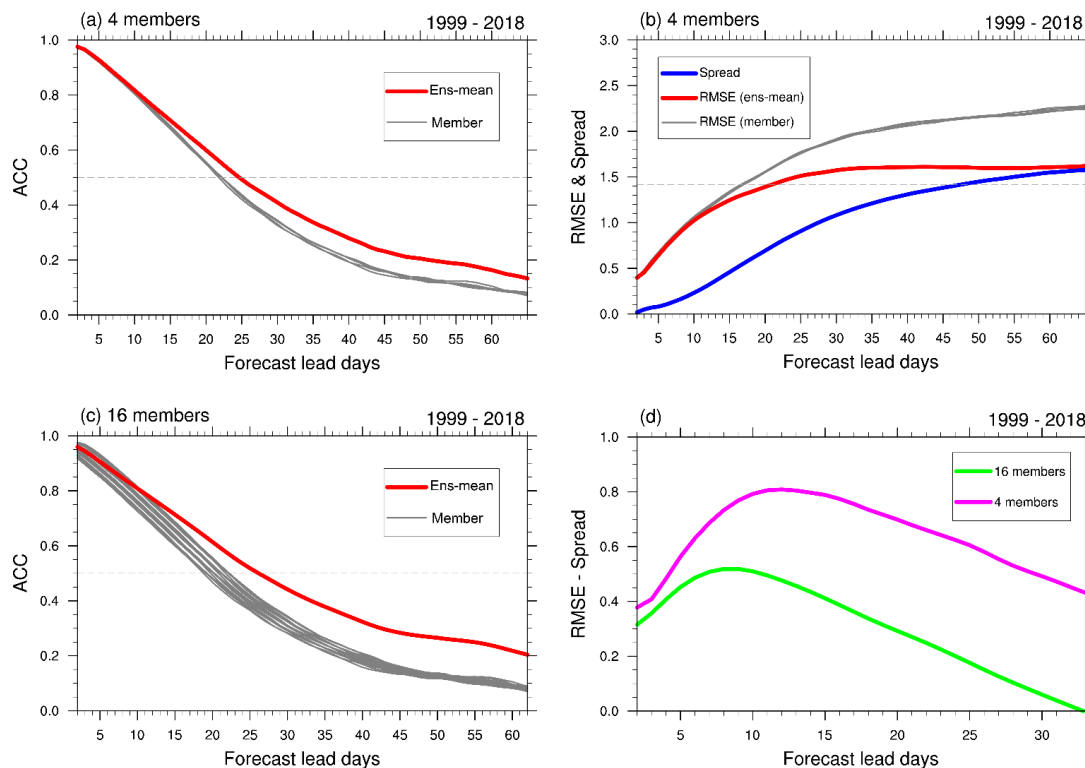
Figure 3. MJO forecast skill of IAP-CAS over 20 years (1999-2018) re-forecast data. (a) The bivariate anomalous correlation
coefficient (ACC) and (b) The Root Mean Squared Error (RMSE) varied with forecast lead days for individual members (gray solid
line) and ensemble mean (red solid line). The blue solid line denotes the ensemble spread. (c) The ACC of individual members and
ensemble mean. The dashed line in (a) and (c) has the values of 0.5, and it represents 1.414 in (b). (d) The difference between RMSE
and Spread of 4-member ensemble mean (purple solid line) and 16-member ensemble mean (green solid line).
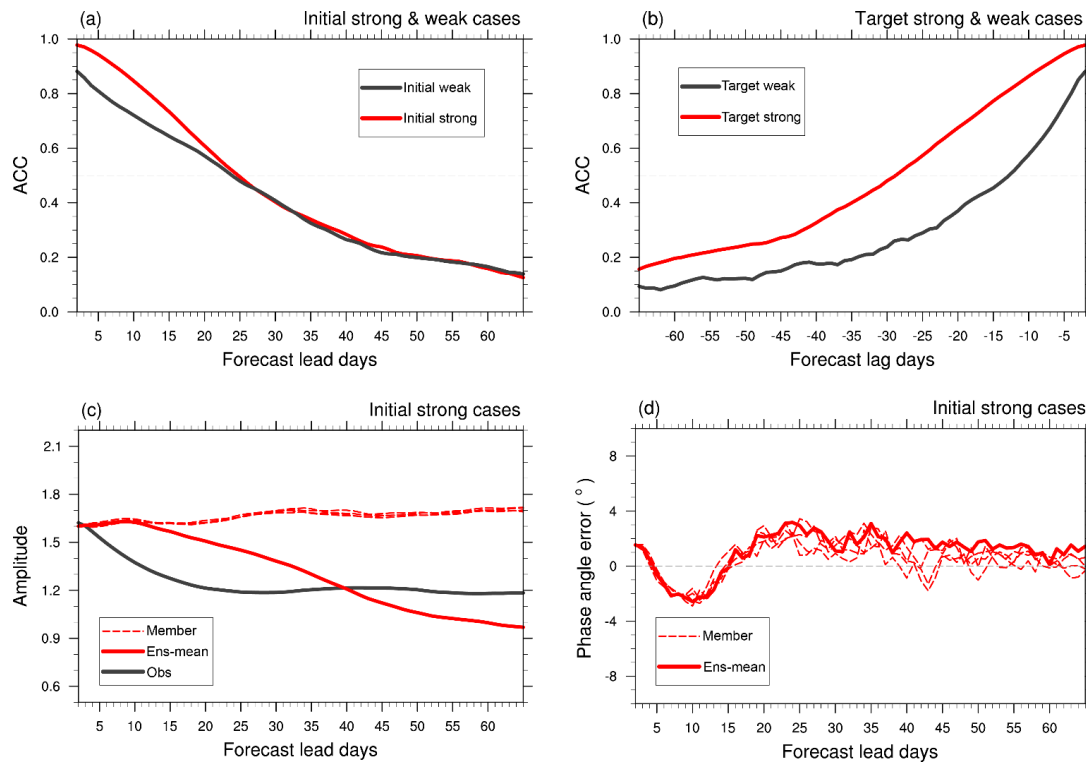
Figure 4. The ACC (a) varied with forecast lead days for initially strong (red) and weak (black) cases and (b) varied with forecast lag days for target strong (red) and weak (black) cases from the ensemble mean. The dashed lines in (a) and (b) have the values of 0.5. (c) The forecast of MJO amplitude varied with forecast lead days for initially strong cases from observation (black solid line), individual ensemble members of the model (red dashed line) and their ensemble mean (red solid line). (d) The forecast of MJO phase angle error (°) for initially strong cases (black solid line). The dashed line in (d) is the reference line with the values of 0.
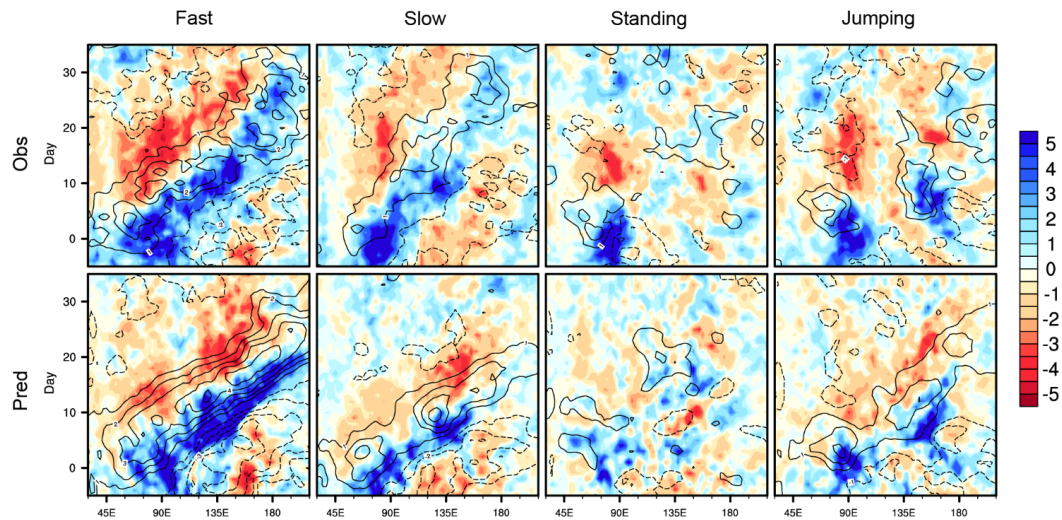
Figure 5. 10° S–10° N averaged Precipitation anomalies (shading; mm day⁻¹) and 850-hPa zonal winds anomalies (contours with an interval of 1 m s⁻¹) varied with longitude (x-axis) and time lag (y-axis; days) composited for four types of MJO. The top row is for observation (NCEP winds and GPCP precipitation), and the bottom row is for model forecasts initiated at day −5 (5 days before the peak day). Solid lines represent positive values and dashed lines represent negative values.
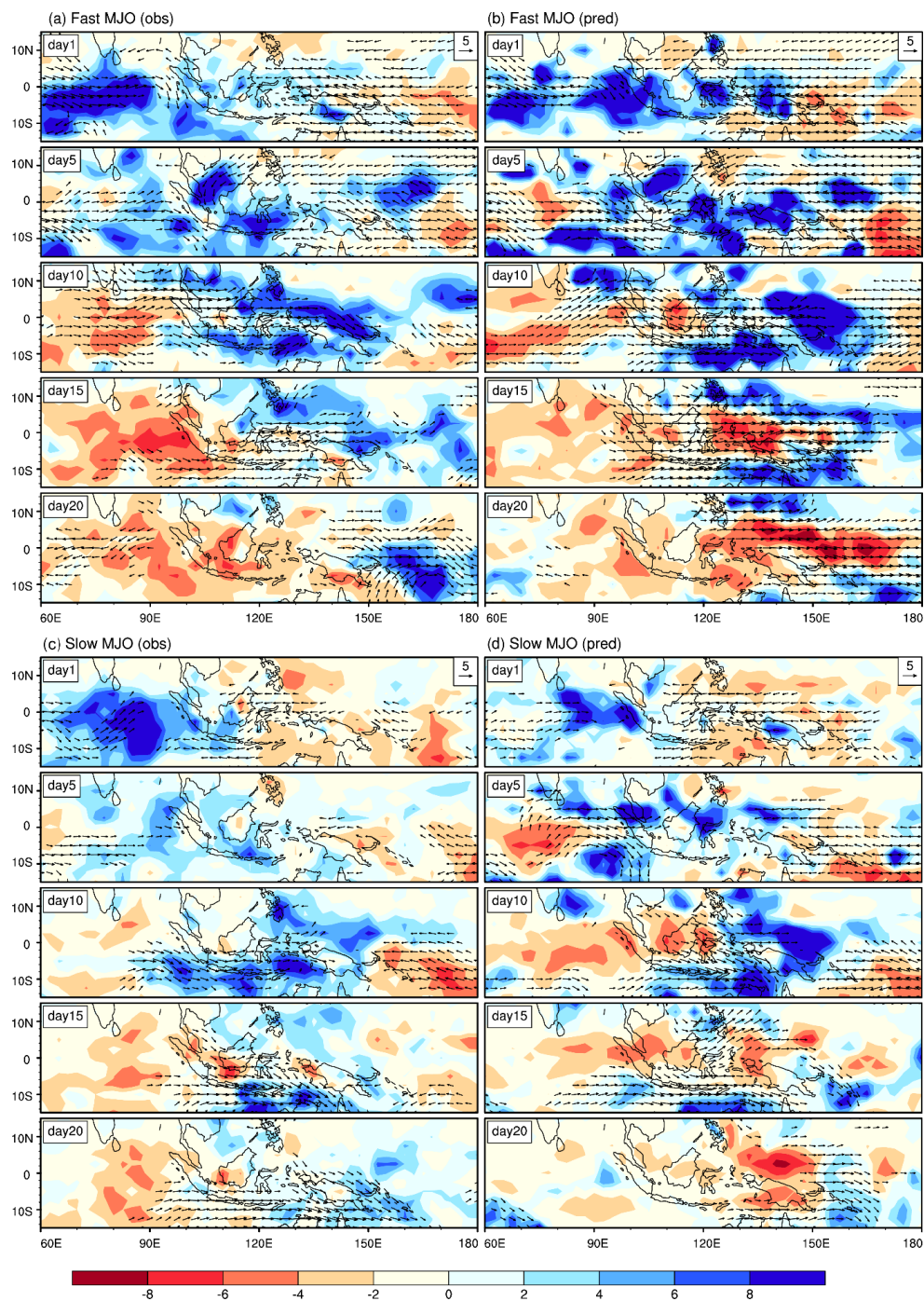
Figure 6. Evolution patterns of the composite precipitation (shading; mm day⁻¹) and 850-hPa winds (vectors; m s⁻¹) anomalies for day 1, day 5, day10, day15 and day 20 in (a) observed fast MJO, (b) simulated fast MJO, (c) observed slow MJO and (d) simulated slow MJO.

477

478 **Figure 7. Composite phase diagrams for (c) fast MJO and (f) slow MJO events from observation (red lines) and IAP-CAS model**

479 **(blue lines). The dots denote every 5 days from the forecast starting date.**
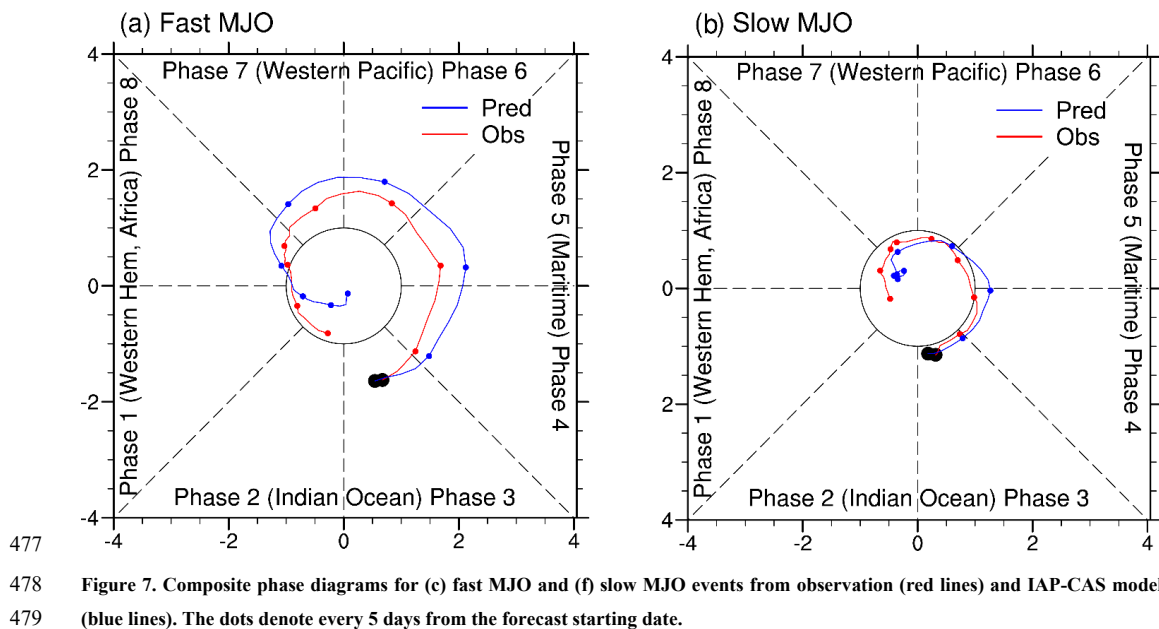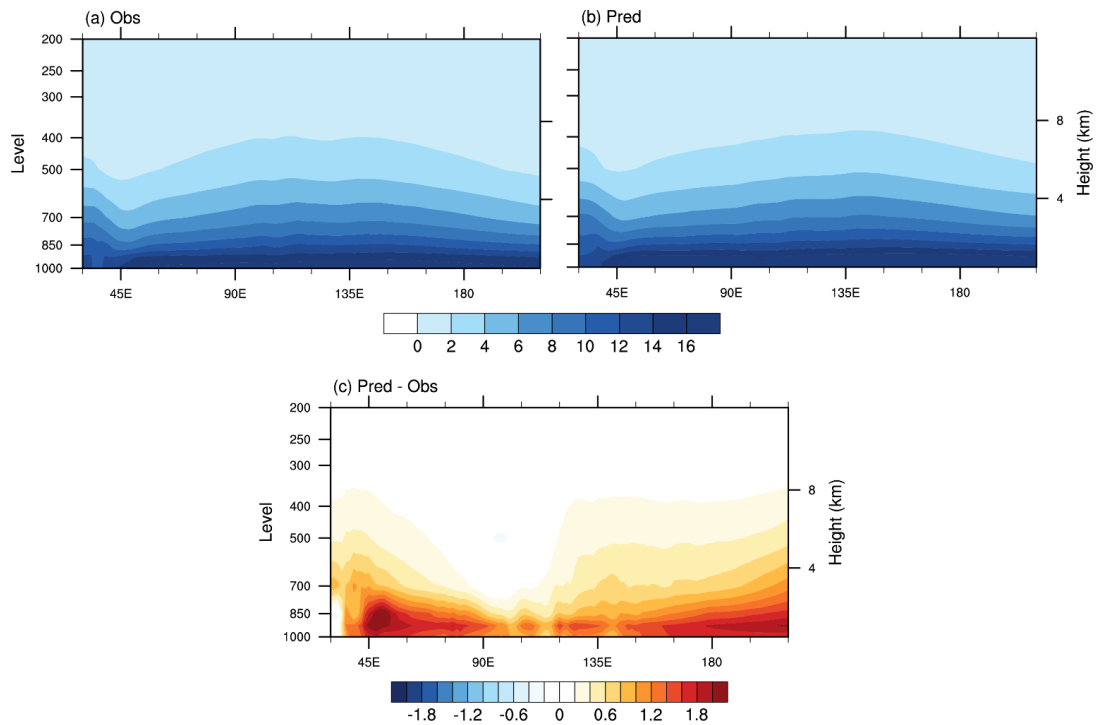
Figure 8. The longitude-vertical profiles of winter (November–April) mean specific humidity (g kg⁻¹) averaged over 10° S–10° N for (a) observation, (b) IAP-CAS model, and (c) the difference between IAP-CAS model and observation.
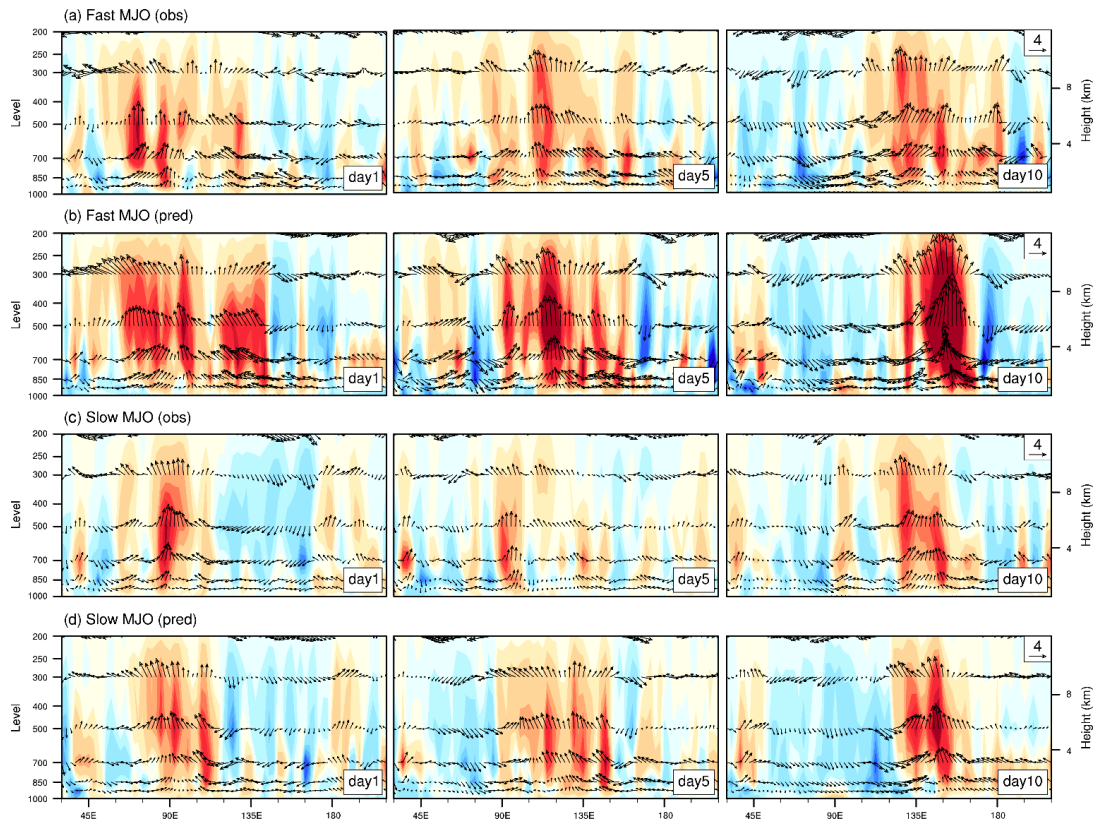
Figure 9. The composited longitude-vertical structure of precipitation heating (contours; 1×10⁻² J kg⁻¹ s⁻¹) and zonal and vertical winds anomalies (vectors; units are m/s for zonal winds and 0.01 Pa s⁻¹ for vertical winds) averaged over 10° S–10° N for day 1, day 5, day 10 in (a) observed fast MJO, (b) simulated fast MJO, (c) observed slow MJO and (b) simulated slow MJO.

Figure 10. The winter (November–April) mean specific humidity (g kg^{-1}) on 850hPa for (a) observation and (b) IAP-CAS model.
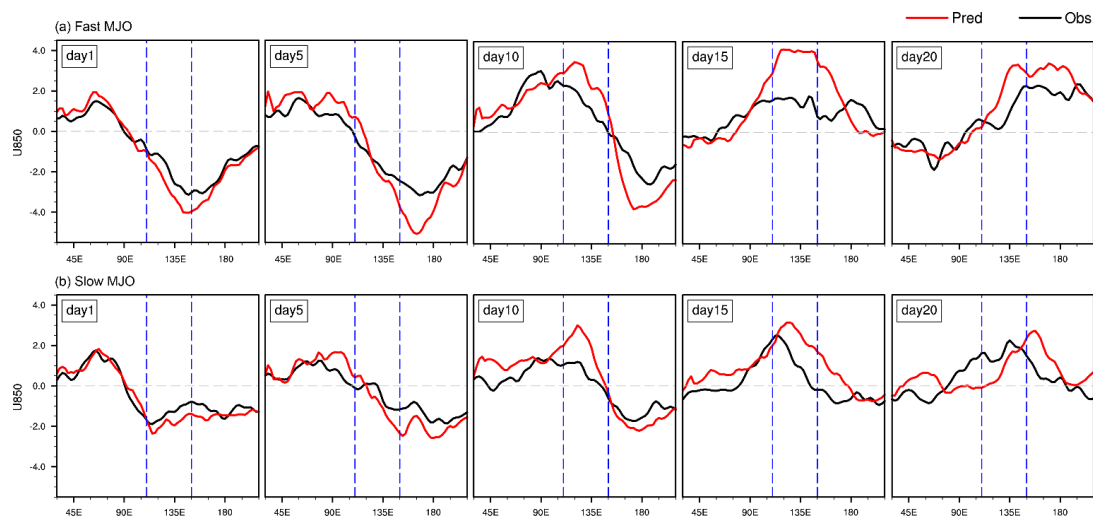
Figure 11. The composited longitudinal structure of the 850hPa zonal wind anomalies (m s⁻¹) averaged over 15° S–15° N for day 1, day 5, day10, day15 and day 20 from observation (black solid line) and IAP-CAS model (red solid line) in fast and slow MJO events. The gray dashed line is the reference line with the values of 0. The two blue dashed lines are 110° E and 150° E respectively, which denote the extension of the MC region.
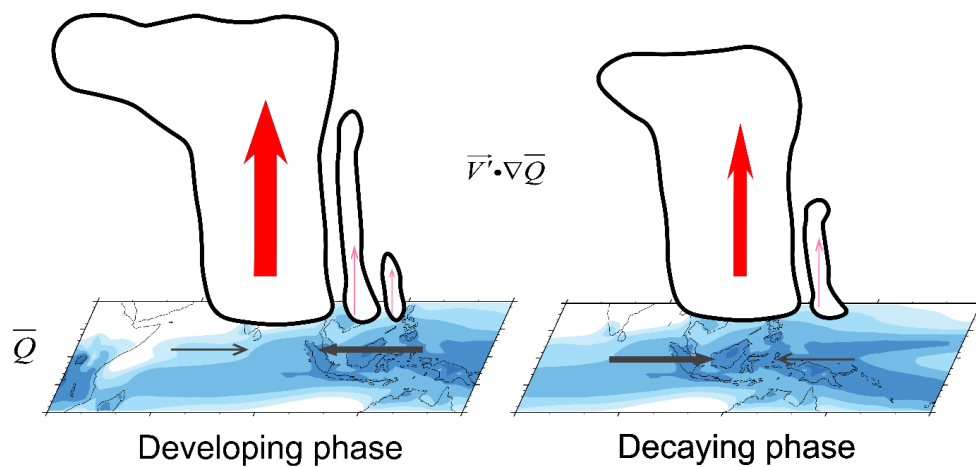
Figure 12. Schematic diagrams illustrating the moisture mode theory on MJO propagation in the MC region.

496
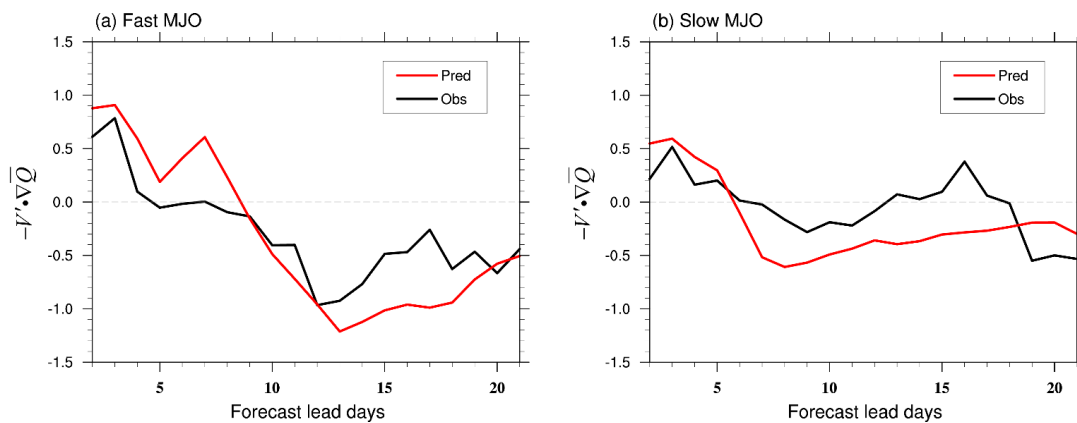
Figure 13. The composited $-V' \cdot \nabla \overline{Q}$ (g kg⁻¹ s⁻¹) averaged over the MC region (15° S-15° N, 110° E-150° E) as a function of forecast lead days from observation (black solid line) and IAP-CAS model (red solid line) in (a) fast MJO and (b) slow MJO events. The gray dashed line is the reference line with the values of 0.
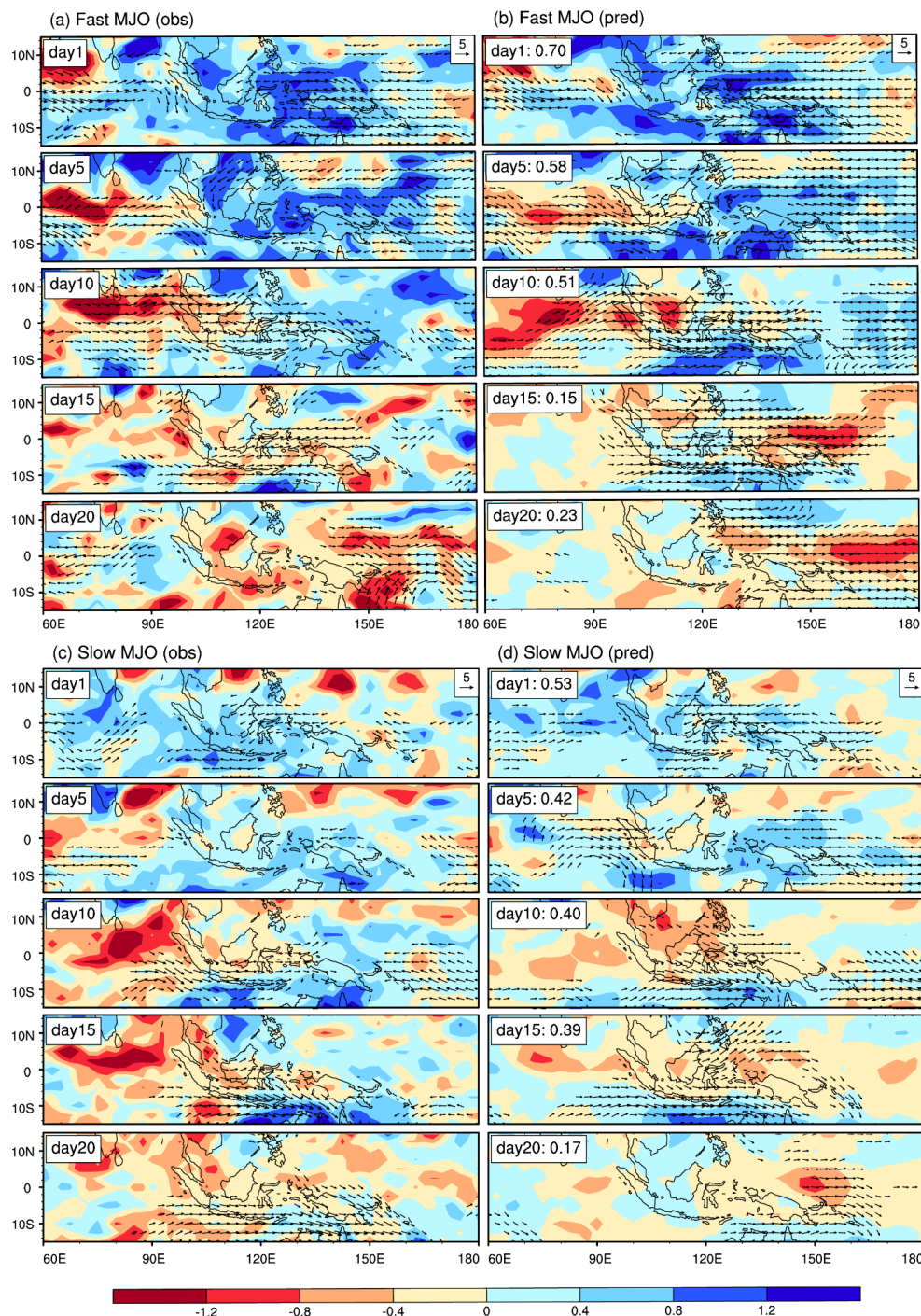
Figure. 14. Evolution patterns of the composite specific humidity anomalies (g kg^{-1}) and winds (vectors; m s^{-1}) anomalies on 850hPa for day 1, day 5, day10, day15 and day 20 (a) observed fast MJO, (b) simulated fast MJO, (c) observed slow MJO and (b) simulated slow MJO. The spatial correlation coefficient between simulated and observed moisture anomalies is shown to the right of panels (b) and (c).

505 **Appendix**
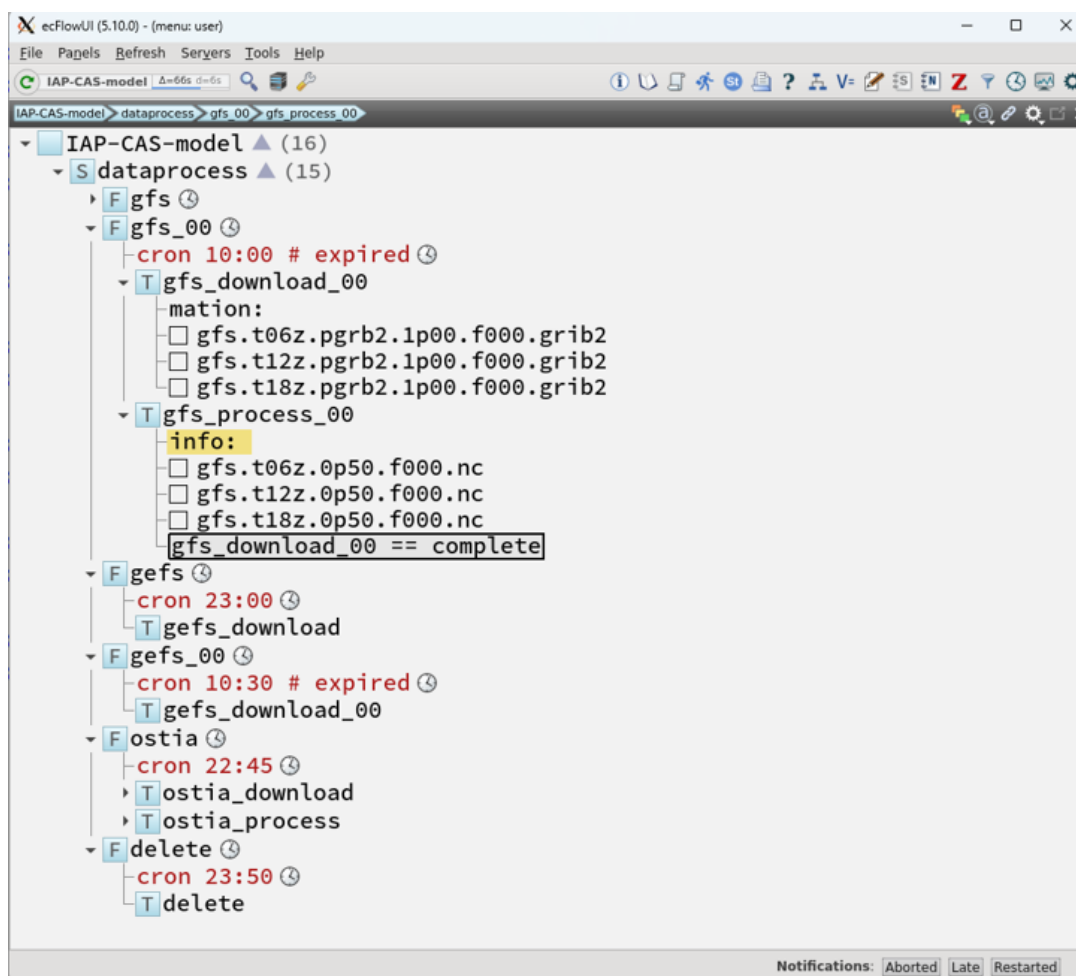
506
507 **Figure A1. The structure of ecFlow (ECMWF Workflow). EcFlow, developed and maintained by the ECMWF, is a client/server**
508 **workflow package designed to facilitate the execution of a substantial number of programs within a controlled environment. It is**
509 **used in the IAP-CAS model to accomplish the download and preprocessing of the forcing data.**
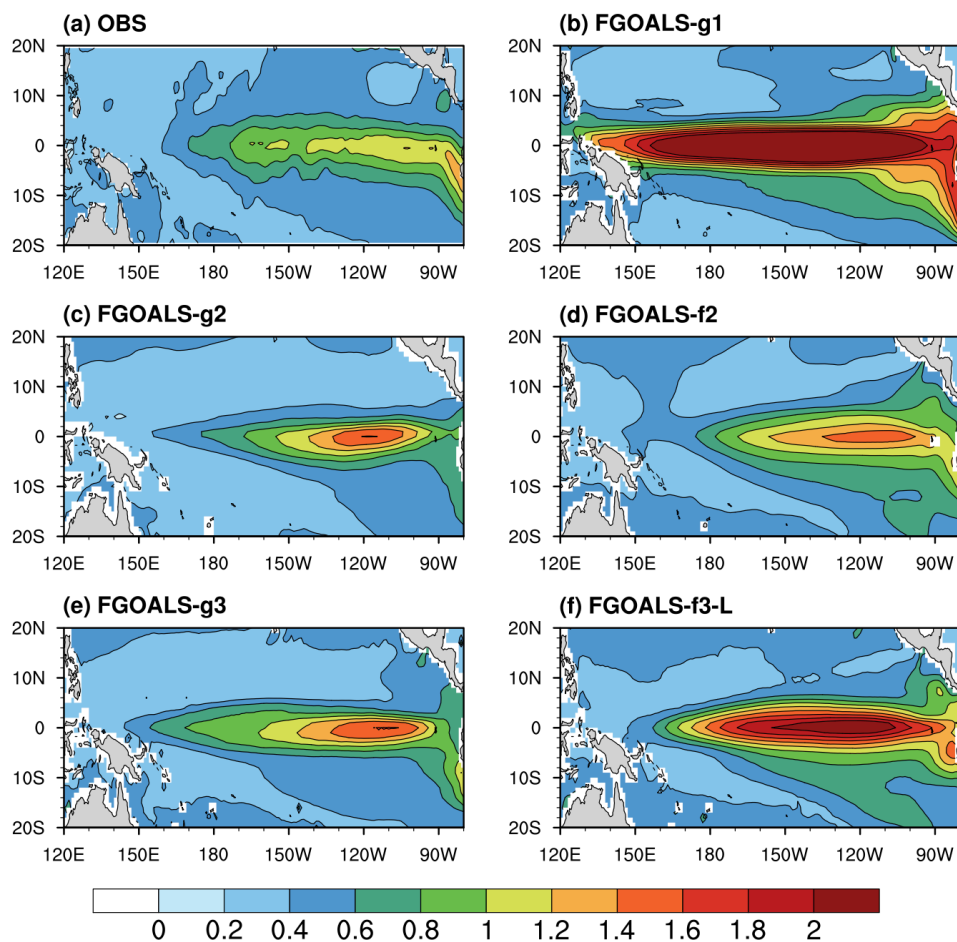
Figure A2. The horizontal distribution of Sea Surface Temperature Anomaly (SSTA) standard deviations in (a) observation and (b)-(e) five FGOALS models from 1948 to 2018.
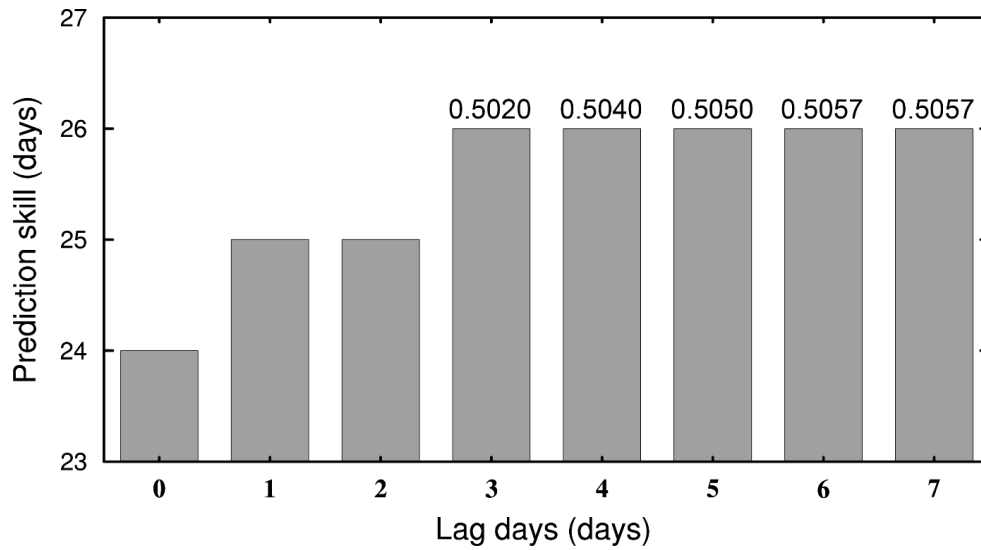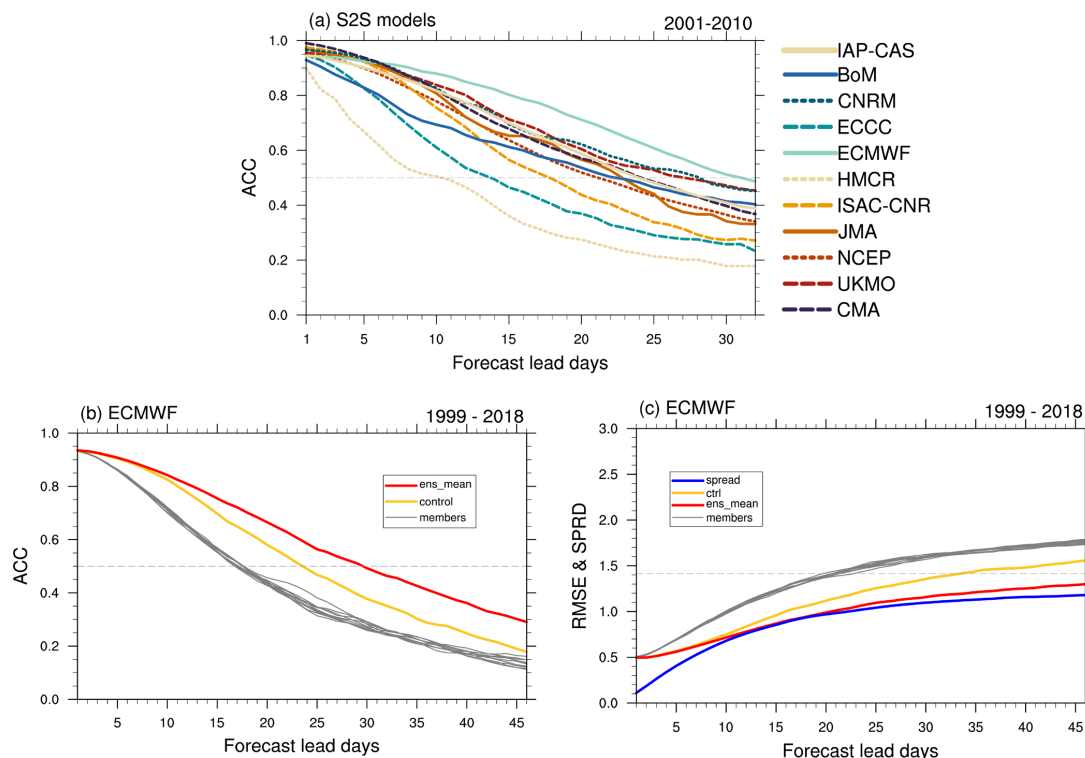
Figure A3. MJO forecast skill of the ensemble mean of time-lagged members as a function of lag days. The values on the bars represent the ACC on day 26.

516
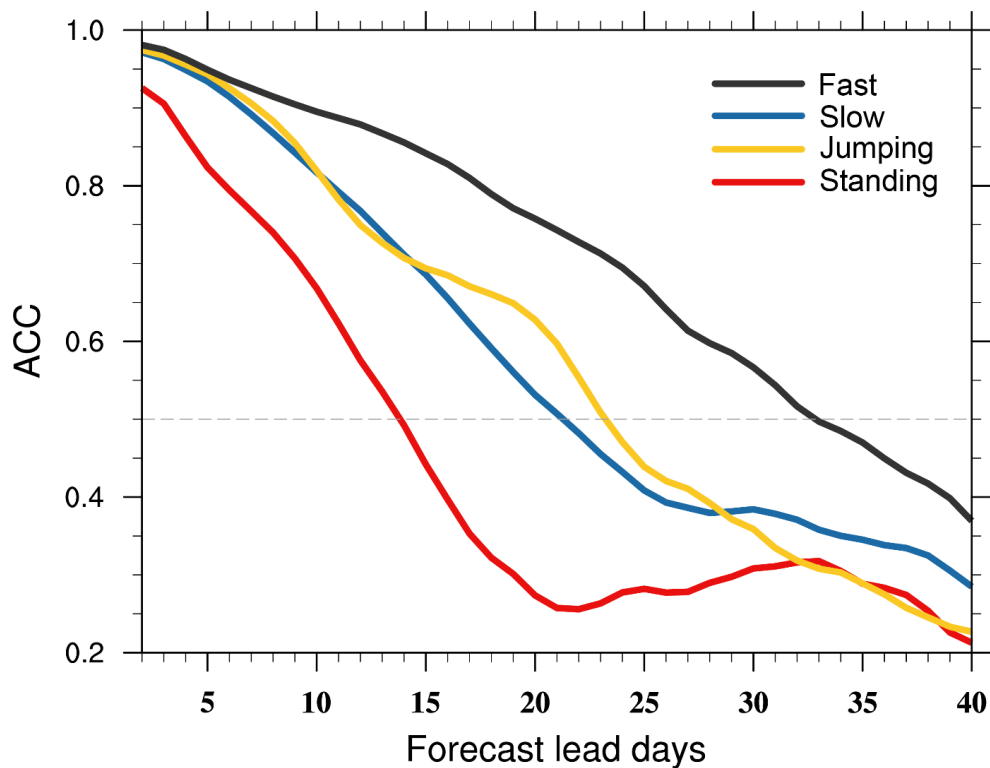
Figure A4. The bivariate ACC as a function of forecast lead days for fast, slow, jumping, and standing MJO events. The dashed line
has the value of 0.5.

Figure A5. MJO forecast skill of S2S models. (a) The ACC between the model ensemble means and ERA-Interim over 10-year (2001-2010) RMM index for 11 S2S models. The datasets used in this study are from the following versions (with the year of update as the version number): IAP-2022, BoM-2014, CNRM-2019, ECCC-2022, ECMWF-2022, HMCR-2022, ISAC-2017, JMA-2020, NCEP-2011, UKMO-2022, CMA-2022. (b) The ACC and (c) the RMSE from individual members (gray solid line), ensemble ctrl (green solid line), and 10-member ensemble mean (red solid line) as a function of forecast lead days. The blue solid line denotes the ensemble spread. The dashed line in (a) and (b) has the values of 0.5, and it represents 1.414 in (c).

Code availability

The code of the IAP-CAS model is archived on Zenodo (https://doi.org/10.5281/zenodo.10791355). The code used to reproduce the figures in this work can be obtained from https://doi.org/10.5281/zenodo.10817813.

Data availability

The boundary conditions and input data are available at https://doi.org/ 10.5281/zenodo.10820243. The data for initial ization in the IAP-CAS S2S system is available at http://rda.ucar.edu/datasets/ds083.2, ds083.2|DOI: 10.5065/D6M043-C6 (FNL), https://www.ncei.noaa.gov/products/optimum-interpolation-sst (NOAA OISST) and https://www.ncei.noaa.go-v/products/weather-climate-models/global-forecast (GFS weather forecast). The hindcast dataset of the IAP-CAS S2S system used in the article is publicly available on the three S2S Data Portals (ECMWF: https://apps.ecmwf.int/data-sets/; CMA: http://s2s.cma.cn/index; IRI: https://iridl.ldeo.columb-ia.edu/SOURCES/ECMWF/S2S/). All the validation data are available to download from the cited references or data links shown in Section 3.1.

Author contribution

Q.B. led the IAP-CAS model development. All other co-authors contributed to it. B.H. and X.F.W. designed the experiments and carried them out. Y.K.L. utilized the dataset to assess the performance of the IAP-CAS S2S system and wrote the final document with contributions from all other authors. Q.B. reviewed and edited the manuscript. G.X.W., Y.M.L., and J.Y. supervised and supported this research and gave important opinions.

Competing interests

The authors declare no conflict of interest.

Acknowledgments

References

Adames, Á. F. and Kim, D.: The MJO as a Dispersive, Convectively Coupled Moisture Wave: Theory and Observations, Journal of the Atmospheric Sciences, 73, 913–941, https://doi.org/10.1175/JAS-D-15-0170.1, 2016.

550   Adames, Á. F. and Wallace, J. M.: Three-Dimensional Structure and Evolution of the MJO and Its Relation to the Mean Flow,

551   Journal of the Atmospheric Sciences, 71, 2007–2026, https://doi.org/10.1175/JAS-D-13-0254.1, 2014.

552   Adames, Á. F. and Wallace, J. M.: Three-Dimensional Structure and Evolution of the Moisture Field in the MJO, Journal of

553   the Atmospheric Sciences, 72, 3733–3754, https://doi.org/10.1175/JAS-D-15-0003.1, 2015.

554   Adler, R. F., Huffman, G. J., Chang, A., Ferraro, R., Xie, P.-P., Janowiak, J., Rudolf, B., Schneider, U., Curtis, S., Bolvin, D.,

555   Gruber, A., Susskind, J., Arkin, P., and Nelkin, E.: The Version-2 Global Precipitation Climatology Project (GPCP) Monthly

556   Precipitation Analysis (1979–Present), Journal of Hydrometeorology, 4, 1147–1167, https://doi.org/10.1175/1525-

557   7541(2003)004<1147:TVGPCP>2.0.CO;2, 2003.

558   Ahn, M., Kim, D., Kang, D., Lee, J., Sperber, K. R., Gleckler, P. J., Jiang, X., Ham, Y., and Kim, H.: MJO Propagation Across

559   the Maritime Continent: Are CMIP6 Models Better Than CMIP5 Models?, Geophysical Research Letters, 47,

560   https://doi.org/10.1029/2020GL087250, 2020.

561   Ahn, M. S., Kim, D., Kang, D., Lee, J., Sperber, K. R., and Gleckler, P. J.: MJO Simulation in CMIP6 Models: How much

562   improvement has been made from CMIP5 to CMIP6?, 2019, A41G-04, 2019.

563   Bao, Q.: Outlook for El Niño and the Indian Ocean Dipole in autumn-winter 2018–2019, CSB, 73–78,

564   https://doi.org/10.1360/N972018-00913, 2019.

565   Bao, Q. and Li, J.: Progress in climate modeling of precipitation over the Tibetan Plateau, National Science Review, 7, 486–

566   487, https://doi.org/10.1093/nsr/nwaa006, 2020.

567   Bao, Q., Liu, Y., Wu, G., He, B., Li, J., Wang, L., Wu, X., Chen, K., Wang, X., Yang, J., and Zhang, X.: CAS FGOALS-f3-

568   H and CAS FGOALS-f3-L outputs for the high-resolution model intercomparison project simulation of CMIP6, Atmospheric

569   and Oceanic Science Letters, 13, 576–581, https://doi.org/10.1080/16742834.2020.1814675, 2020.

570   Benedict, J. J. and Randall, D. A.: Observed Characteristics of the MJO Relative to Maximum Rainfall, Journal of the

571   Atmospheric Sciences, 64, 2332–2354, https://doi.org/10.1175/JAS3968.1, 2007.

572   Bessafi, M. and Wheeler, M. C.: Modulation of south Indian ocean tropical cyclones by the Madden-Julian oscillation and

573   convectively coupled equatorial waves, Mon. Weather Rev., 134, 638–656, https://doi.org/10.1175/MWR3087.1, 2006.

574   Cassou, C.: Intraseasonal interaction between the Madden–Julian Oscillation and the North Atlantic Oscillation, Nature, 455,

575   523–527, https://doi.org/10.1038/nature07286, 2008.

576   Chen, G., Ling, J., Zhang, R., Xiao, Z., and Li, C.: The MJO From CMIP5 to CMIP6: Perspectives From Tracking MJO

577   Precipitation, Geophysical Research Letters, 49, https://doi.org/10.1029/2021GL095241, 2022.

578   Craig, A. P., Vertenstein, M., and Jacob, R.: A new flexible coupler for earth system modeling developed for CCSM4 and

579   CESM1, The International Journal of High Performance Computing Applications, 26, 31–42,

580   https://doi.org/10.1177/1094342011428141, 2012.

581   Crueger, T., Stevens, B., and Brokopf, R.: The Madden-Julian Oscillation in ECHAM6 and the Introduction of an Objective

582   MJO Metric, J. Clim., 26, 3241–3257, https://doi.org/10.1175/JCLI-D-12-00413.1, 2013.

583   DeMott, C. A., Wolding, B. O., Maloney, E. D., and Randall, D. A.: Atmospheric Mechanisms for MJO Decay Over the

584   Maritime Continent, Journal of Geophysical Research: Atmospheres, 123, 5188–5204, https://doi.org/10.1029/2017JD026979,

585   2018.

586   ERA, C.: Fifth generation of ECMWF atmospheric reanalyses of the global climate, Copernicus Climate Change Service

587   Climate Data Store (CDS), 2017.

588   Fan, Y., Yang, J., Li, J., Qi, X., and Bao, Q.: Gain of one-month lead predicting spring rainfall over China: A comparison

589   between FGOALS-f2 ensemble prediction system and its driving stretched-grid downscaling prediction system, Atmospheric

590   Research, 283, 106570, https://doi.org/10.1016/j.atmosres.2022.106570, 2023.

591   Ferreira, R. N., Schubert, W. H., and Hack, J. J.: Dynamical aspects of twin tropical cyclones associated with the Madden-

592   Julian oscillation, J. Atmos. Sci., 53, 929–945, https://doi.org/10.1175/1520-0469(1996)053<0929:DAOTTC>2.0.CO;2, 1996.

593   Gonzalez, A. O. and Jiang, X.: Winter mean lower tropospheric moisture over the Maritime Continent as a climate model

594   diagnostic metric for the propagation of the Madden-Julian oscillation, Geophysical Research Letters, 44, 2588–2596,

595   https://doi.org/10.1002/2016GL072430, 2017.

596   Goswami, B. N.: South asian monsoon, Springer, 2012.

597   Gottschalck, J., Wheeler, M., Weickmann, K., Vitart, F., Savage, N., Lin, H., Hendon, H., Waliser, D., Sperber, K., Nakagawa,

598   M., Prestrelo, C., Flatau, M., and Higgins, W.: A Framework for Assessing Operational Madden–Julian Oscillation Forecasts:

599   A CLIVAR MJO Working Group Project, Bull. Amer. Meteor. Soc., 91, 1247–1258,

600   https://doi.org/10.1175/2010BAMS2816.1, 2010.

601   Hall, J. D., Matthews, A. J., and Karoly, D. J.: The modulation of tropical cyclone activity in the Australian region by the

602   Madden-Julian oscillation, Mon. Weather Rev., 129, 2970–2982, https://doi.org/10.1175/1520-

603   0493(2001)129<2970:TMOTCA>2.0.CO;2, 2001.

604   Hannah, W. M., Maloney, E. D., and Pritchard, M. S.: Consequences of systematic model drift in DYNAMO MJO hindcasts

605   with SP-CAM and CAM5, Journal of Advances in Modeling Earth Systems, 7, 1051–1074,

606   https://doi.org/10.1002/2014MS000423, 2015.

607   Harris, L., Zhou, L., Lin, S.-J., Chen, J.-H., Chen, X., Gao, K., Morin, M., Rees, S., Sun, Y., Tong, M., Xiang, B., Bender, M.,

608   Benson, R., Cheng, K.-Y., Clark, S., Elbert, O. D., Hazelton, A., Huff, J. J., Kaltenbaugh, A., Liang, Z., Marchok, T., Shin, H.

609   H., and Stern, W.: GFDL SHiELD: A Unified System for Weather-to-Seasonal Prediction, Journal of Advances in Modeling

610   Earth Systems, 12, e2020MS002223, https://doi.org/10.1029/2020MS002223, 2020.

611   Harris, L. M. and Lin, S.-J.: A Two-Way Nested Global-Regional Dynamical Core on the Cubed-Sphere Grid, Monthly

612   Weather Review, 141, 283–306, https://doi.org/10.1175/MWR-D-11-00201.1, 2013.

613   Hendon, H. H. and Salby, M. L.: The Life Cycle of the Madden–Julian Oscillation, Journal of the Atmospheric Sciences, 51,

614   2225–2237, https://doi.org/10.1175/1520-0469(1994)051<2225:TLCOTM>2.0.CO;2, 1994.

615   Ho, C.-H., Kim, J.-H., Jeong, J.-H., Kim, H.-S., and Chen, D.: Variation of tropical cyclone activity in the South Indian Ocean:

616   El Niño–Southern Oscillation and Madden-Julian Oscillation effects, J. Geophys. Res., 111, D22101,

617   https://doi.org/10.1029/2006JD007289, 2006.

618   Hoffman, R. N. and Kalnay, E.: Lagged average forecasting, an alternative to Monte Carlo forecasting, Tellus A: Dynamic

619   Meteorology and Oceanography, 35, 100–118, https://doi.org/10.3402/tellusa.v35i2.11425, 1983.

620   Hsu, H. H. and Lee, M. Y.: Topographic effects on the eastward propagation and initiation of the Madden-Julian oscillation,

621   J. Clim., 18, 795–809, https://doi.org/10.1175/JCLI-3292.1, 2005.

622   Hsu, H.-H.: Intraseasonal variability of the atmosphere–ocean–climate system: East Asian monsoon, in: Intraseasonal

623   Variability in the Atmosphere-Ocean Climate System, edited by: Lau, W. K.-M. and Waliser, D. E., Springer Berlin Heidelberg,

624   Berlin, Heidelberg, 73–110, https://doi.org/10.1007/978-3-642-13914-7_3, 2012.

625   Hsu, P. and Li, T.: Role of the Boundary Layer Moisture Asymmetry in Causing the Eastward Propagation of the Madden–

626   Julian Oscillation, Journal of Climate, 25, 4914–4931, https://doi.org/10.1175/JCLI-D-11-00310.1, 2012.

627   Hung, M.-P., Lin, J.-L., Wang, W., Kim, D., Shinoda, T., and Weaver, S. J.: MJO and Convectively Coupled Equatorial Waves

628   Simulated by CMIP5 Climate Models, Journal of Climate, 26, 6185–6214, https://doi.org/10.1175/JCLI-D-12-00541.1, 2013.

629   Hunke, E. C., Lipscomb, W. H., Turner, A. K., Jeffery, N., and Elliott, S.: Cice: the los alamos sea ice model documentation

630   and software user's manual version 4.1 la-cc-06-012, T-3 Fluid Dynamics Group, Los Alamos National Laboratory, 675, 500,

631   2010.

632   Inness, P. M. and Slingo, J. M.: The interaction of the Madden-Julian Oscillation with the Maritime Continent in a GCM, Q.

633   J. R. Meteorol. Soc., 132, 1645–1667, https://doi.org/10.1256/qj.05.102, 2006.

634   Jeuken, A. B. M., Siegmund, P. C., Heijboer, L. C., Feichter, J., and Bengtsson, L.: On the potential of assimilating

635   meteorological analyses in a global climate model for the purpose of model validation, Journal of Geophysical Research:

636   Atmospheres, 101, 16939–16950, https://doi.org/10.1029/96JD01218, 1996.

637   Jiang, X.: Key processes for the eastward propagation of the Madden-Julian Oscillation based on multimodel simulations: Key

638   Model Processes for MJO Propagation, J. Geophys. Res. Atmos., 122, 755–770, https://doi.org/10.1002/2016JD025955, 2017.

639   Jiang, X., Adames, Á. F., Zhao, M., Waliser, D., and Maloney, E.: A Unified Moisture Mode Framework for Seasonality of

640   the Madden–Julian Oscillation, Journal of Climate, 31, 4215–4224, https://doi.org/10.1175/JCLI-D-17-0671.1, 2018.

641   Kanamitsu, M., Ebisuzaki, W., Woollen, J., Yang, S.-K., Hnilo, J. J., Fiorino, M., and Potter, G. L.: NCEP–DOE AMIP-II

642   Reanalysis (R-2), Bulletin of the American Meteorological Society, 83, 1631–1644, https://doi.org/10.1175/BAMS-83-11-

643   1631, 2002.

644   Kemball-Cook, S. R. and Weare, B. C.: The Onset of Convection in the Madden–Julian Oscillation, J. Climate, 14, 780–793,

645   https://doi.org/10.1175/1520-0442(2001)014<0780:TOOCIT>2.0.CO;2, 2001.

646   Kerbyson, D. J. and Jones, P. W.: A Performance Model of the Parallel Ocean Program, The International Journal of High

647   Performance Computing Applications, 19, 261–276, https://doi.org/10.1177/1094342005056114, 2005.

648   Kim, D., Kug, J.-S., and Sobel, A. H.: Propagating versus Nonpropagating Madden–Julian Oscillation Events, Journal of

649   Climate, 27, 111–125, https://doi.org/10.1175/JCLI-D-13-00084.1, 2014a.

650   Kim, H.: MJO Propagation Processes and Mean Biases in the SubX and S2S Reforecasts, J. Geophys. Res. Atmos., 124, 9314–

651   9331, https://doi.org/10.1029/2019JD031139, 2019.

652   Kim, H., Vitart, F., and Waliser, D. E.: Prediction of the Madden–Julian Oscillation: A Review, J Climate, 31, 9425–9443,

653   https://doi.org/10.1175/JCLI-D-18-0210.1, 2018.

654   Kim, H.-M.: The impact of the mean moisture bias on the key physics of MJO propagation in the ECMWF reforecast, Journal

655   of Geophysical Research: Atmospheres, 122, 7772–7784, https://doi.org/10.1002/2017JD027005, 2017.

656   Kim, H.-M., Webster, P. J., Toma, V. E., and Kim, D.: Predictability and Prediction Skill of the MJO in Two Operational

657   Forecasting Systems, J Climate, 27, 5364–5378, https://doi.org/10.1175/JCLI-D-13-00480.1, 2014b.

658   Lau, K.-M. and Chan, P. H.: Aspects of the 40–50 Day Oscillation during the Northern Summer as Inferred from Outgoing

659   Longwave   Radiation,   Monthly   Weather   Review,   114,   1354–1367,   https://doi.org/10.1175/1520-

660   0493(1986)114<1354:AOTDOD>2.0.CO;2, 1986.

661   Lau, W. K., Waliser, D. E., and Lau, W. K.: El Nino southern oscillation connection, Springer, 2005.

662   Lawrence, D. M., Oleson, K. W., Flanner, M. G., Thornton, P. E., Swenson, S. C., Lawrence, P. J., Zeng, X., Yang, Z.-L.,

663   Levis, S., Sakaguchi, K., Bonan, G. B., and Slater, A. G.: Parameterization improvements and functional and structural

664   advances in Version 4 of the Community Land Model: PARAMETERIZATION IMPROVEMENTS AND FUNCTIONAL

665   AND STRUCTURAL ADVANCES, J. Adv. Model. Earth Syst., 3, n/a-n/a, https://doi.org/10.1029/2011MS00045, 2011.

666   Leutbecher, M. and Palmer, T. N.: Ensemble forecasting, Journal of Computational Physics, 227, 3515–3539,

667   https://doi.org/10.1016/j.jcp.2007.02.014, 2008.

668   Li, J., Bao, Q., Liu, Y., Wu, G., Wang, L., He, B., Wang, X., and Li, J.: Evaluation of FAMIL2 in Simulating the Climatology

669   and Seasonal-to-Interannual Variability of Tropical Cyclone Characteristics, J. Adv. Model. Earth Syst., 11, 1117–1136,

670   https://doi.org/10.1029/2018MS001506, 2019.

671   Li, J., Bao, Q., Liu, Y., Wu, G., Wang, L., He, B., Wang, X., Yang, J., Wu, X., and Shen, Z.: Dynamical Seasonal Prediction

672   of Tropical Cyclone Activity Using the FGOALS-f2 Ensemble Prediction System, Weather and Forecasting, 36, 1759–1778,

673   https://doi.org/10.1175/WAF-D-20-0189.1, 2021.

674   Li, J., Tian, Q., Shen, Z., Yan, Z., Li, M., Xue, J., Yang, Y., Zeng, L., Zang, Y., and Li, S.: Evaluation of Dynamical Seasonal

675   Prediction Skills for Tropical Cyclone Activity over the South China Sea in FGOALS-f2, Atmosphere, 14, 85,

676   https://doi.org/10.3390/atmos14010085, 2022.

677   Liebmann, B. and Smith, C. A.: Description of a Complete (Interpolated) Outgoing Longwave Radiation Dataset, Bulletin of

678   the American Meteorological Society, 77, 1275–1277, 1996.

679   Liebmann, B., Hendon, H., and Glick, J.: The Relationship Between Tropical Cyclones of the Western Pacific and Indian

680   Oceans and the Madden-Julian Oscillation, J. Meteorol. Soc. Jpn., 72, 401–412, https://doi.org/10.2151/jmsj1965.72.3_401,

681   1994.

682   Lim, Y., Son, S.-W., and Kim, D.: MJO Prediction Skill of the Subseasonal-to-Seasonal Prediction Models, Journal of Climate,

683   31, 4075–4094, https://doi.org/10.1175/JCLI-D-17-0545.1, 2018.

684   Lin, H., Brunet, G., and Derome, J.: Forecast Skill of the Madden–Julian Oscillation in Two Canadian Atmospheric Models,

685   Monthly Weather Review, 136, 4130–4149, https://doi.org/10.1175/2008MWR2459.1, 2008.

686   Lin, S.-J.: A "Vertically Lagrangian" Finite-Volume Dynamical Core for Global Models, Monthly Weather Review, 132,

687   2293–2307, https://doi.org/10.1175/1520-0493(2004)132<2293:AVLFDC>2.0.CO;2, 2004.

688   Lin, Y., Farley, R., and Orville, H.: Bulk Parameterization of the Snow Field in a Cloud Model, JOURNAL OF CLIMATE

689   AND APPLIED METEOROLOGY, 22, 1065–1092, https://doi.org/10.1175/1520-0450(1983)022<1065:BPOTSF>2.0.CO;2,

690   1983.

691   Liu, A., Yang, J., Bao, Q., He, B., Wu, X., Liu, J., Kim, S.-J., and Fan, Y.: Subseasonal-to-seasonal prediction of arctic sea ice

692   Using a Fully Coupled dynamical ensemble forecast system, Atmospheric Research, 295, 107014,

693   https://doi.org/10.1016/j.atmosres.2023.107014, 2023.

694   Liu, Y. Q.: Prediction of monthly-seasonal precipitation using coupled SVD patterns between soil moisture and subsequent

695   precipitation, Geophys. Res. Lett., 30, 1827, https://doi.org/10.1029/2003GL017709, 2003.

696   Lorenz, E. N.: Predictability: A problem partly solved, in Proceedings of Seminar on Predictability, 4–8 September 1995, 1996.

697   Madden, R. A. and Julian, P. R.: Detection of a 40–50 Day Oscillation in the Zonal Wind in the Tropical Pacific, Journal of

698   the Atmospheric Sciences, 28, 702–708, https://doi.org/10.1175/1520-0469(1971)028<0702:DOADOI>2.0.CO;2, 1971.

699   Maloney, E. D.: An Intraseasonal Oscillation Composite Life Cycle in the NCAR CCM3.6 with Modified Convection, J.

700   Climate, 15, 964–982, https://doi.org/10.1175/1520-0442(2002)015<0964:AIOCLC>2.0.CO;2, 2002.

701   Maloney, E. D. and Hartmann, D. L.: Modulation of eastern North Pacific hurricanes by the Madden-Julian oscillation, J.

702   Clim., 13, 1451–1460, https://doi.org/10.1175/1520-0442(2000)013<1451:MOENPH>2.0.CO;2, 2000.

703   Mu, M., Duan, W. S., and Wang, B.: Conditional nonlinear optimal perturbation and its applications, Nonlinear Processes in

704   Geophysics, 10, 493–501, https://doi.org/10.5194/npg-10-493-2003, 2003.

705   Nasuno, T., Li, T., and Kikuchi, K.: Moistening Processes before the Convective Initiation of Madden–Julian Oscillation

706   Events during the CINDY2011/DYNAMO Period, Monthly Weather Review, 143, 622–643, https://doi.org/10.1175/MWR-

707   D-14-00132.1, 2015.

708   Neena, J. M., Lee, J. Y., Waliser, D., Wang, B., and Jiang, X.: Predictability of the Madden–Julian Oscillation in the

709   Intraseasonal Variability Hindcast Experiment (ISVHE)*, J Climate, 27, 4531–4543, https://doi.org/10.1175/JCLI-D-13-

710   00624.1, 2014.

711   Nerger, L., Tang, Q., and Mu, L.: Efficient ensemble data assimilation for coupled models with the Parallel Data Assimilation

712   Framework: example of AWI-CM (AWI-CM-PDAF 1.0), Geosci. Model Dev., 13, 4305–4321, https://doi.org/10.5194/gmd-

713   13-4305-2020, 2020.

714   Oleson, W., Lawrence, M., Bonan, B., Flanner, G., Kluzek, E., Lawrence, J., Levis, S., Swenson, C., Thornton, E., Dai, A.,

715   Decker, M., Dickinson, R., Feddema, J., Heald, L., Hoffman, F., Lamarque, J.-F., Mahowald, N., Niu, G.-Y., Qian, T.,

716   Randerson, J., Running, S., Sakaguchi, K., Slater, A., Stockli, R., Wang, A., Yang, Z.-L., Zeng, X., and Zeng, X.: Technical

717   Description of version 4.0 of the Community Land Model (CLM), https://doi.org/10.5065/D6FB50WZ, 2010.

718   Park, S. and Bretherton, C. S.: The University of Washington Shallow Convection and Moist Turbulence Schemes and Their

719   Impact on Climate Simulations with the Community Atmosphere Model, J. Clim., 22, 3449–3469,

720   https://doi.org/10.1175/2008JCLI2557.1, 2009.

721   Pham, D. T.: Stochastic Methods for Sequential Data Assimilation in Strongly Nonlinear Systems, Mon. Wea. Rev., 129,

722   1194–1207, https://doi.org/10.1175/1520-0493(2001)129<1194:SMFSDA>2.0.CO;2, 2001.

723   Putman, W. M. and Lin, S.-J.: Finite-volume transport on various cubed-sphere grids, Journal of Computational Physics, 227,

724   55–78, https://doi.org/10.1016/j.jcp.2007.07.022, 2007.

725   Rashid, H. A., Hendon, H. H., Wheeler, M. C., and Alves, O.: Prediction of the Madden–Julian oscillation with the POAMA

726   dynamical prediction system, Clim Dynam, 36, 649–661, https://doi.org/10.1007/s00382-010-0754-x, 2011.

727   Raymond, D. J. and Fuchs, Ž.: Moisture Modes and the Madden–Julian Oscillation, Journal of Climate, 22, 3031–3046,

728   https://doi.org/10.1175/2008JCLI2739.1, 2009.

729   Reynolds, R. W., Smith, T. M., Liu, C., Chelton, D. B., Casey, K. S., and Schlax, M. G.: Daily High-Resolution-Blended

730   Analyses for Sea Surface Temperature, Journal of Climate, 20, 5473–5496, https://doi.org/10.1175/2007JCLI1824.1, 2007.

731   Rui, H. and Wang, B.: Development Characteristics and Dynamic Structure of Tropical Intraseasonal Convection Anomalies,

732   Journal of the Atmospheric Sciences, 47, 357–379, https://doi.org/10.1175/1520-0469(1990)047<0357:DCADSO>2.0.CO;2,

733   1990a.

734   Rui, H. and Wang, B.: Development Characteristics and Dynamic Structure of Tropical Intraseasonal Convection Anomalies,

735   Journal of the Atmospheric Sciences, 47, 357–379, https://doi.org/10.1175/1520-0469(1990)047<0357:DCADSO>2.0.CO;2,

736   1990b.

737   Vitart, F.: Madden—Julian Oscillation prediction and teleconnections in the S2S database, Q.J.R. Meteorol. Soc, 143, 2210–

738   2220, https://doi.org/10.1002/qj.3079, 2017.

739   Vitart, F. and Molteni, F.: Dynamical Extended-Range Prediction of Early Monsoon Rainfall over India, Mon. Weather Rev.,

740   137, 1480–1492, https://doi.org/10.1175/2008MWR2761.1, 2009.

741   Vitart, F. and Molteni, F.: Simulation of the Madden-Julian Oscillation and its teleconnections in the ECMWF forecast system,

742   Q. J. R. Meteorol. Soc., 136, 842–855, https://doi.org/10.1002/qj.623, 2010.

743   Vitart, F., Ardilouze, C., Bonet, A., Brookshaw, A., Chen, M., Codorean, C., Déqué, M., Ferranti, L., Fucile, E., Fuentes, M.,

744   Hendon, H., Hodgson, J., Kang, H.-S., Kumar, A., Lin, H., Liu, G., Liu, X., Malguzzi, P., Mallas, I., Manoussakis, M.,

745   Mastrangelo, D., MacLachlan, C., McLean, P., Minami, A., Mladek, R., Nakazawa, T., Najm, S., Nie, Y., Rixen, M., Robertson,

746   A. W., Ruti, P., Sun, C., Takaya, Y., Tolstykh, M., Venuti, F., Waliser, D., Woolnough, S., Wu, T., Won, D.-J., Xiao, H.,

747   Zaripov, R., and Zhang, L.: The Subseasonal to Seasonal (S2S) Prediction Project Database, B Am Meteorol Soc, 98, 163–

748   173, https://doi.org/10.1175/BAMS-D-16-0017.1, 2017.

749   Waliser, D. E., Lau, K. M., Stern, W., and Jones, C.: Potential Predictability of the Madden–Julian Oscillation, B Am Meteorol

750   Soc, 84, 33–50, https://doi.org/10.1175/BAMS-84-1-33, 2003.

751   Wang, B.: Dynamics of Tropical Low-Frequency Waves: An Analysis of the Moist Kelvin Wave, Journal of the Atmospheric

752   Sciences, 45, 2051–2065, https://doi.org/10.1175/1520-0469(1988)045<2051:DOTLFW>2.0.CO;2, 1988.

753   Wang, B. and Lee, S.-S.: MJO Propagation Shaped by Zonal Asymmetric Structures: Results from 24 GCM Simulations,

754   Journal of Climate, 30, 7933–7952, https://doi.org/10.1175/JCLI-D-16-0873.1, 2017.

755   Wang, B., Chen, G., and Liu, F.: Diversity of the Madden-Julian Oscillation, SCIENCE ADVANCES, 2019.

756   Wang, W., Hung, M.-P., Weaver, S. J., Kumar, A., and Fu, X.: MJO prediction in the NCEP Climate Forecast System version

757   2, Clim Dyn, 42, 2509–2520, https://doi.org/10.1007/s00382-013-1806-9, 2014.

758   Wheeler, M. C. and Hendon, H. H.: An All-Season Real-Time Multivariate MJO Index: Development of an Index for

759   Monitoring and Prediction, Monthly Weather Review, 132, 1917–1932, https://doi.org/10.1175/1520-

760   0493(2004)132<1917:AARMMI>2.0.CO;2, 2004a.

761   Wheeler, M. C. and Hendon, H. H.: An All-Season Real-Time Multivariate MJO Index: Development of an Index for

762   Monitoring and Prediction, Mon. Wea. Rev., 132, 1917–1932, https://doi.org/10.1175/1520-

763   0493(2004)132<1917:AARMMI>2.0.CO;2, 2004b.

764   Wheeler, M. C., Hendon, H. H., Cleland, S., Meinke, H., and Donald, A.: Impacts of the Madden–Julian Oscillation on

765   Australian Rainfall and Circulation, Journal of Climate, 22, 1482–1498, https://doi.org/10.1175/2008JCLI2595.1, 2009.

766   Wu, C.-H. and Hsu, H.-H.: Topographic Influence on the MJO in the Maritime Continent, J. Clim., 22, 5433–5448,

767   https://doi.org/10.1175/2009JCLI2825.1, 2009.

768   Wu, X., Deng, L., Song, X., Vettoretti, G., Peltier, W. R., and Zhang, G. J.: Impact of a modified convective scheme on the

769   Madden-Julian Oscillation and El Niño-Southern Oscillation in a coupled climate model: MJO AND ENSO SIMULATED

770   BY A COUPLED GCM, Geophys. Res. Lett., 34, https://doi.org/10.1029/2007GL030637, 2007.

771   Xiang, B., Zhao, M., Jiang, X., Lin, S.-J., Li, T., Fu, X., and Vecchi, G.: The 3–4-Week MJO Prediction Skill in a GFDL

772   Coupled Model, J Climate, 28, 5351–5364, https://doi.org/10.1175/JCLI-D-15-0102.1, 2015.

773   Xiang, B., Harris, L., Delworth, T. L., Wang, B., Chen, G., Chen, J.-H., Clark, S. K., Cooke, W. F., Gao, K., Huff, J. J., Jia,

774   L., Johnson, N. C., Kapnick, S. B., Lu, F., McHugh, C., Sun, Y., Tong, M., Yang, X., Zeng, F., Zhao, M., Zhou, L., and Zhou,

775   X.: S2S Prediction in GFDL SPEAR: MJO Diversity and Teleconnections, B Am Meteorol Soc, 103, E463–E484,

776   https://doi.org/10.1175/BAMS-D-21-0124.1, 2022.

777   Yang, C., Liu, J., and Xu, S.: Seasonal Arctic Sea Ice Prediction Using a Newly Developed Fully Coupled Regional Model

778   With the Assimilation of Satellite Sea Ice Observations, J Adv Model Earth Syst, 12, e2019MS001938,

779   https://doi.org/10.1029/2019MS001938, 2020.

780   Zeng, L., Bao, Q., Wu, X., He, B., Yang, J., Wang, T., Liu, Y., Wu, G., and Liu, Y.: Impacts of humidity initialization on MJO

781   prediction: A study in an operational sub-seasonal to seasonal system, Atmospheric Research, 294, 106946,

782   https://doi.org/10.1016/j.atmosres.2023.106946, 2023.

783   Zhang, C.: Madden-Julian Oscillation: MADDEN-JULIAN OSCILLATION, Rev. Geophys., 43,

784   https://doi.org/10.1029/2004RG000158, 2005.

785   Zhou, L. and Harris, L.: Integrated Dynamics-Physics Coupling for Weather to Climate Models: GFDL SHiELD With In-Line

786   Microphysics, Geophys. Res. Lett., 49, e2022GL100519, https://doi.org/10.1029/2022GL100519, 2022.

787   Zhou, L., Lin, S.-J., Chen, J.-H., Harris, L. M., Chen, X., and Rees, S. L.: Toward Convective-Scale Prediction within the Next

788   Generation Global Prediction System, Bulletin of the American Meteorological Society, 100, 1225–1243,

789   https://doi.org/10.1175/BAMS-D-17-0246.1, 2019.